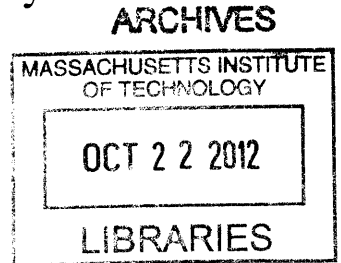


Direct and Quantitative Broadband Absorptance
Micro/Nano Spectroscopy Using FTIR and Bilayer
Cantilever Probes

by
Wei-Chun Hsu



Submitted to the Department of Mechanical Engineering
in partial fulfillment of the requirements for the degree of

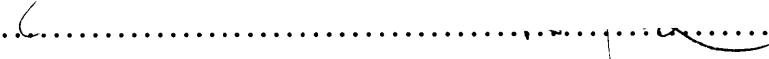
Master of Science in Mechanical Engineering

at the

MASSACHUSETTS INSTITUTE OF TECHNOLOGY

September 2012

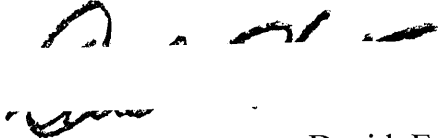
© Massachusetts Institute of Technology 2012. All rights reserved.

Author.....

Department of Mechanical Engineering
August 2, 2012

Certified by.....

Gang Chen
Carl Richard Soderberg Professor of Power Engineering
Thesis Supervisor

Accepted by.....

David E. Hardt
Chairman, Department Committee on Graduate Students

Direct and Quantitative Broadband Absorptance Micro/Nano Spectroscopy Using FTIR and Bilayer Cantilever Probes

By

Wei-Chun Hsu

Submitted to the Department of Mechanical Engineering
on August 2, 2012, in partial fulfillment of the
requirements for the degree of
Master of Science in Mechanical Engineering

Abstract

Optical properties of micro/nano materials are important for many applications in biology, optoelectronics, and energy. In this thesis, a method is described to directly measure the quantitative absorptance spectra of micro/nano-sized structures using Fourier Transform Spectroscopy (FTS). The measurement technique combines optomechanical cantilever probes with a modulated broadband light source from an interferometer for spectroscopic measurements of objects. Previous studies have demonstrated the use of bilayer (or multi-layer) cantilevers as highly sensitive heat flux probes with the capability of resolving power as small as ~ 4 pW. Fourier Transform Spectroscopy is a well-established method to measure broadband spectra with significant advantages over conventional dispersive spectrometers such as a higher power throughput and large signal-to-noise ratio for a given measurement time. By integrating a bilayer cantilever probe with a Michelson interferometer, the new platform is capable of measuring broadband absorptance spectra from $3\mu\text{m}$ to $18\mu\text{m}$ directly and quantitatively with an enhanced sensitivity that enables the characterization of micro- and nanometer-sized samples, which cannot be achieved by using conventional spectroscopic techniques. Besides, a paralleled project of a bi-armed cantilever decouples the sample arm and the probe arm to further enhance the signal-to-noise ratio.

Thesis Supervisor: Gang Chen

Title: Carl Richard Soderberg Professor of Power Engineering

Dedication

To my family, Chung-Lin Lu, and my friends.

Acknowledgements

The completion of this thesis belongs to numerous individuals. First, I would like to thank my thesis' advisor, Prof. Gang Chen, for providing me an opportunity to work on the new idea of micro and nanometer-sized spectroscopy and for offering funding and the patient discussions. Second, I need to share the completion of this project with my collaborators, Bolin Liao, Jonathan Tong, and Brian Burg. Bolin helped me construct the major modeling analysis and assemble the experimental system. Jonathan Tong taught me to set up the optics and related equipment, and helped me with troubleshooting. Brian Burg designed and fabricated the bi-armed cantilever that is used in this new application, and he also taught me the fabrication process. Third, I want to show my appreciation to my labmates and friends, Shuo Chen, Daniel Kraemer, Jiun-Yih Kuan, I-Hsin Pan, Shien-Ping Feng, Tz-How Huang, Wen-Chien Chen, Kuang-Han Chu, Chih-Hung Hsieh, Selçuk Yerci, Andrej Lenert, George Ni, Poetro Sambegoro, Austin Minnich, Andy Muto, Kimberlee Collins, Maria Luckyanova, Kenneth McEnaney, Vazrik Chiloyan, Lee Weinstein, Matthew Branham, Sohae Kim, Sangyeop Lee, Jianjian Wang, Qin Ling, Yan Zhou, and Zhiting Tian. They are being with me and help me in a very important stage of my MIT life.

Contents

1 Introduction

- 1.1 Fourier Transform Spectroscopy
- 1.2 Micro-fabricated Bilayer Cantilever
- 1.3 Micro/Nano Spectroscopy
- 1.4 Summary

2 System and Operating Principle of the Direct and Quantitative Broadband

Absorptance Micro/Nano Spectroscopy

- 2.1 System
- 2.2 Michelson interferometer
- 2.3 Fiber Optics
- 2.4 Dynamic Behavior of the Bilayer Cantilever
 - 2.4.1 Frequency Response of Temperature
 - 2.4.2 Frequency Response of Deflection
 - 2.4.3 Three Fitted Properties

3 Calibrations for Quantitative Measurements

- 3.1 Background Spectrum Calibration
- 3.2 Beam Intensity Distribution Calibration
- 3.3 Frequency Response Calibration
- 3.4 Power Calibration

3.5 Total Calibration Factor

4 Experimental Validation

4.1 Absorptance of Si/Al thin films

4.2 Raw Data

4.3 Data Calibrations

4.4 Summary and Results

5 Conclusion

5.1 Summary

5.2 Extension of Prior Art

5.3 Future Work

List of Figures

Figure 1-1 Schematic diagram of the photoacoustic cell.....	19
Figure 1-2 Schematic diagram of a bilayer cantilever.	20
Figure 1-3 A micro-spectroscopy using a micrometer-sized thermocouple probe and a Fourier transform infrared system.....	23
Figure 1-4 Nano IR system using a tunable pulsed infrared source and an atomic force microscope tip	24
Figure 1-5 Nano-FTIR using a Michelson interferometer and a scattering-type scanning near-field optical microscopy	25
Figure 2-1 Schematic of the system in this thesis combing a light source assembly and a detector and probe assembly.....	29
Figure 2-2 Bending of a bilayer cantilever beam due to a temperature change.....	30
Figure 2-3 Different sample and probe configurations of decoupled cantilever arms.....	30
Figure 2-4 Operating principle of the Michelson interferometer.....	32
Figure 2-5 A simulated interferogram pattern from a Michelson interferometer.....	34
Figure 2-6 Operating principle of the fiber.....	35
Figure 2-7 Transmission of the polycrystalline infra-red fiber	37
Figure 2-8 Intensity of the polycrystalline infra-red fiber.....	38
Figure 2-9 Gaussian function fitting of the intensity distribution of the polycrystalline	

infra-red fiber.....	38
Figure 2-10 Least squares method fitting for the standard deviation of σ of the Gaussian function.....	39
Figure 2-11 Schematic of the coordinate system and the differential element under uniformly heating.....	41
Figure 2-12 Schematic of the coordinate system and the differential element under the tip heating.....	44
Figure 2-13 Frequency response of temperature of the Si/Al bilayer cantilever with total power of $1 \mu W$	45
Figure 2-14 Schematic of the coordinate system and the free body diagram of the bilayer cantilever.....	48
Figure 2-15 Deflection frequency responses of the bilayer cantilever with uniform heating calculated with different effective Young's modulus.....	53
Figure 2-16 Deflection frequency responses of the bilayer cantilever with uniform heating calculated with different damping coefficients.....	53
Figure 2-17 Deflection frequency responses of the bilayer cantilever with uniform heating calculated with convective heat transfer coefficients.....	54
Figure 2-18 Deflection frequency responses of the bilayer cantilever with tip heating calculated with different effective Young's modulus.....	54
Figure 2-19 Deflection frequency responses of the bilayer cantilever with tip heating calculated with different damping coefficients.....	55
Figure 2-20 Deflection frequency responses of the bilayer cantilever with tip heating calculated with convective heat transfer coefficients.....	55
Figure 3-1 Incident power spectrum exiting from the polycrystalline infra-red fiber.....	58
Figure 3-2 Background spectra measured by a Fourier transform infrared system with	

different B-stop values.....	60
Figure 3-3 Schematic of the beam intensity distribution calibration.....	61
Figure 3-4 Two dimensional intensity profile	62
Figure 3-5 Two dimensional incident intensity on the cantilever	62
Figure 3-6 Incident input power spectrum after background and beam intensity distribution calibrations	63
Figure 3-7 Experimental and theoretical frequency response of the Si/Al cantilever	64
Figure 3-8 Operating range of frequency response of the bilayer Si/Al cantilever	65
Figure 3-9 System configuration used in the power calibration.	66
Figure 3-10 Experimental setups for the power calibration.....	67
Figure 3-11 Frequency response of the Si/Al cantilever after the power calibration..	67
Figure 4-1 Absorptance of the silicon/aluminum thin film with different doping concentration.....	70
Figure 4-2 Absorptance of the silicon/aluminum thin film with different thickness of the silicon layer.....	70
Figure 4-3 Deflection signals of the Si/Al cantilever in time domain captured by the position sensitive detector with different velocities of mirror.....	72
Figure 4-4 Absorption spectra of the Si/Al cantilever with different velocities of mirror	73
Figure 4-5 Background spectra of the Si/Al cantilever.....	73
Figure 4-6 Absorption spectra of the Si/Al cantilever after subtracting the background spectrum.....	74
Figure 4-7 Absolute absorbed power spectra of the Si/Al cantilever after the frequency response calibration.....	76

Figure 4-8 Absorptance spectra with the theoretical calculation and experimental measurements of different velocities.....	77
Figure 4-9 Flow diagram of the calibrations.....	78
Figure 4-10 Averaged absorptance of experimental measurements with the theoretical calculation.....	79
Figure 5-1 SiNx/Au bi-arm cantilever sensor.....	83

List of Tables

Table 1. The thermal and dimensional properties of the silicon/aluminum cantilever.....	43
Table 2. The mechanical properties of the silicon/aluminum cantilever.....	52
Table 3. The fiber power estimated by the FTIR and thermopile.....	59
Table 4. The error of each measurement.....	80

Chapter 1

Introduction

Optical properties of micro/nano materials are important for many applications in biology, optoelectronics, and energy harvesting. Fourier Transform Spectroscopy is a well-developed system to measure optical information such as the reflectance and transmittance, while the absorptance is calculated by subtracting of reflectance and transmittance from unity. However, the spectroscopy on micro and nanometer-sized samples needs a new solution. In 1994, Gimzewski used a bilayer cantilever to sense chemical reactions about 1 pJ, which opened a direction for absorption measurements on micro and nanometer-sized objects.^{1,2} This thesis demonstrates a new method of measuring absorptance directly and quantitatively by combining Fourier transform infrared spectroscopy and a bilayer cantilever probes.

1.1 Fourier Transform Spectroscopy

Fourier transform infrared (FTIR) and Fourier transform visible (FTVIS) spectroscopy, referred to as Fourier Transform Spectroscopy (FTS) in general, are well-known techniques to measure the optical properties of materials.³ FTS uses the

Michelson interferometer to realize the broadband spectra. By using different sample stages, FTIR and FTVIS systems can measure the transmittance and reflectance spectra of a sample. Compared to dispersive spectrometers, FTIR and FTVIS have several important advantages. First, the multiplex advantage (or Fellgett advantage) implies that FTIR and FTVIS systems can simultaneously measure all wavelengths in the illumination source. Thus a complete spectrum can be collected in a single scan faster than for conventional dispersive spectrometers. Second, the throughput advantage (or Jacquinot advantage) refers to the higher energy throughput of FTIR and FTVIS systems compared to dispersive spectrometers which results in a higher signal-to-noise ratio for the same spectral resolution. Third, since FTIR and FTVIS system use an interferometer to modulate the spectrum instead of prisms or gratings, stray light is negligible unlike in dispersive spectrometers.

Traditional methods to measure an absorbance spectrum, including FTIR and FTVIS, are typically indirect, in the sense that the absorbance spectrum of materials can only be calculated after measuring the transmittance and reflectance spectrum. This approach inevitably introduces uncertainties and errors in the result. For bulk materials, indirect methods are usually adequate to determine absorption characteristics, qualitatively or even quantitatively. For small samples on the micro or nanometer scale, however, it is difficult to use the FTS method to characterize the absorption spectrum, since the light scattered by the sample is often unaccounted for.

One direct absorption measurement method using FTIR and FTVIS is based on photoacoustic. Fig. 1-1 shows the structure of the Uotila's photoacoustic cell.^{4,5,6} Due to the modulated infrared (IR) intensity of FTIR, the temperature of the surrounded gas oscillates. This oscillating temperature generates the pressure wave inside the sample chamber, and the vibration can be detected by the cantilever-typed microphone and directly relates to the absorption power; however, the photoacoustic

cell has difficulties in measuring small samples and calibrating its signal to absolute power.

The direct measurements have benefits that indirect measurements cannot have. First, indirect methods subtract the reflectance and transmittance from unity to estimate the absorptance. Scattering light can generate errors especially for small samples. In contrast, direct methods are not affected by scattering. Second, reflectance measurement restricts the incident angle because of the space of the light source and the detector, but direct methods can easily measure the absorptance at normal incident. Nevertheless, no matter the direct or indirect methods, the absorption on micro and nanometer-sized samples require a new tool to detect power of nanowatts or even picowatts. We address this challenge using microfabricated bilayer cantilever in a photothermal measurement.

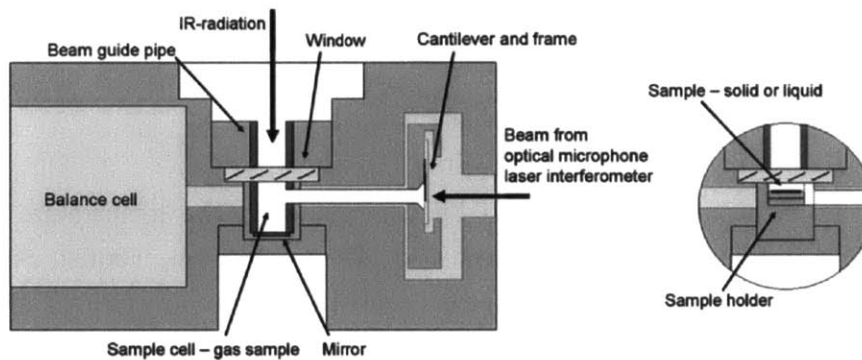


Figure 1-1 : Schematic diagram of the photoacoustic cell. The photoacoustic cell with a sample cell for the gas (left) and a sample cell for solid and liquid (right). Modulated infrared (IR) radiations are incident on top of the sample cell. Heat absorbed by the sample generates the pressure wave due to the change of temperature, and the cantilever-typed microphone detects the pressure wave to reconstruct the absorption property of the sample.

1.2 Micro-fabricated Bilayer Cantilever

The operating principle of the bilayer cantilever was demonstrated by Timoshenko in 1925.⁷ When a cantilever consists of two layers of materials with different thermal expansion coefficients, it bends under the influence of temperature change. Fig. 1-2 shows the schematic diagram.⁸

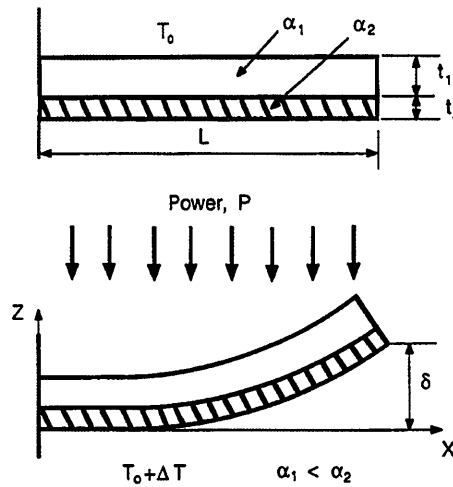


Figure 1-2 : Schematic diagram of a bilayer cantilever. The temperature change induces the bending of a bilayer cantilever due to different thermal expansion coefficients of the two layers. The upper figure shows the structure of a bilayer cantilever at the initial temperature, and the lower figure shows the cantilever bending due to the temperature change.

The small deflection length in steady state under linear approximation due to the temperature change can be described by

$$\frac{d^2 z}{dx^2} = 6(\alpha_2 - \alpha_1) \cdot \frac{t_1 + t_2}{t_2^2 K} \cdot [T(x) - T_0] \quad (1)$$

where

$$K = 4 + 6 \cdot \left(\frac{t_1}{t_2}\right) + 4 \cdot \left(\frac{t_1}{t_2}\right)^2 + \left(\frac{E_1}{E_2}\right) \cdot \left(\frac{t_1}{t_2}\right)^3 + \left(\frac{E_2}{E_1}\right) \cdot \left(\frac{t_2}{t_1}\right) \quad (2)$$

T_0 and ΔT are the initial temperature and the temperature change of the bilayer cantilever respectively. α_1 and α_2 are the thermal expansion coefficients of material 1 and 2. t_1 and t_2 are the thicknesses of material 1 and 2. L is the total length. P is the heating power in Fig. 1-2. Z is the deflection length due to the temperature change. X is the coordinate.

Micro-fabricated bilayer cantilevers have been used as direct and quantitative thermal sensors with an ultra-high power resolution. As photothermal sensors (or a heat flux sensors), micro-cantilevers have reported high sensitivities to detect a minimum power as low as 4 pW.^{1,9,10,11} After carrying out appropriate calibrations, the cantilevers can be used to extract quantitative data,^{12,13,14} and they have been used to measure the thin film thermal conductance,¹² near-field thermal radiation,¹³ absorbance of a thin gold film,¹⁴ absorption of a few isolated chemical materials,^{15,16} specific protein conformations,¹⁷ and thermal conductivity of polyethylene nanofibers.¹⁸ In these works, only steady or quasi-steady (combining the lock-in amplifier) deflection of the bilayer cantilever are applied to measure power quantitatively; however, the broadband spectroscopy is feasible by integrating FTS with the dynamic deflection of the bilayer cantilever, which is not achieved in these cited papers.

1.3 Micro/Nano Spectroscopy

Ever since the invention of the microfabricated cantilever, many kinds of micro/nano spectroscopy techniques using microfabricated cantilevers have been demonstrated to measure the absorption property of micro/nanometer-sized samples or local regions such as polymers and bacteria.^{19,20,21,22,23} In particular, micrometer-sized thermocouples or Atomic Force Microscopy (AFM) cantilevers have shown a spatial resolution in the range of micro/nanometer. In this section, the thermocouple approach, Nano IR system, and Nano-FTIR system are reviewed and differentiated from the new technique that will be proposed in this thesis.

The thermocouple approach is shown on the right of Fig. 1-3.^{19,20} The principle of this approach is to use a micrometer-sized thermocouple to detect the local temperature variation of a sample due to the modulated heating from an FTIR system. This method has been used to detect the absorption spectra of the poly-(butylene terephthalate), polycarbonate, polypropylene, and polyamide, and the results agreed with the spectra measured by the conventional attenuated total reflection infrared spectroscopy.^{19,20} The 5 μm thermocouple probe on the left of Fig. 1-3 offers electrical readings based on the temperature difference between the tip and the environment. This approach can allow a broadband spectrum measurement, but the sensitivity of the thermocouple does not allow measurement of the absorption of micro/nanoscale objects. Samples heated by the IR sources are usually bulky in size.

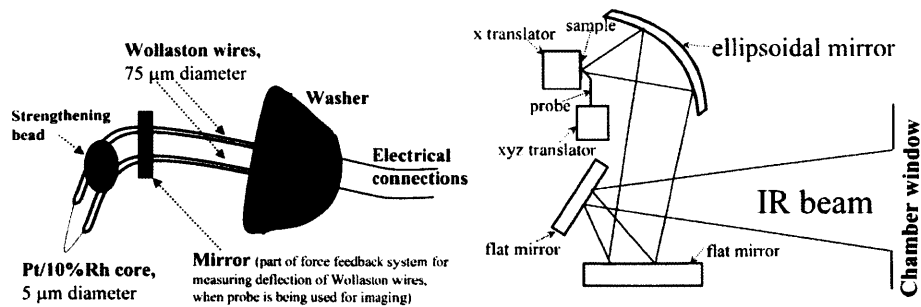


Figure 1-3 : A micro-spectroscopy using a micrometer-sized thermocouple probe and a Fourier transform infrared system. The left figure shows the structure of the micrometer-sized thermocouple probe. The right figure shows the schematic of the whole system. Figures adapted from Ref.19 and 20.

Nano IR system uses the AFM tip to measure the thickness variation of the sample due to the thermal expansion (Fig. 1-4).^{21,22} A modulated, pulsed, and tunable infrared source from 2.5 μm to 10 μm is used to heat up the sample, and the fast Fourier transform of the reflected signal from cantilever provides the information of spectral absorptions. This technique allows a nanoscale local measurement depending on the size of the AFM tip, and this system has been used to detect the qualitative absorption spectra of the resin and bacteria of *Escherichia coli*.^{21,22} In this technique, samples to be measured are deposited on a substrate, and absolute absorptance measurement is difficult due to complicated and often unknown heat transfer and thermal expansion relation of the sample with the substrate.

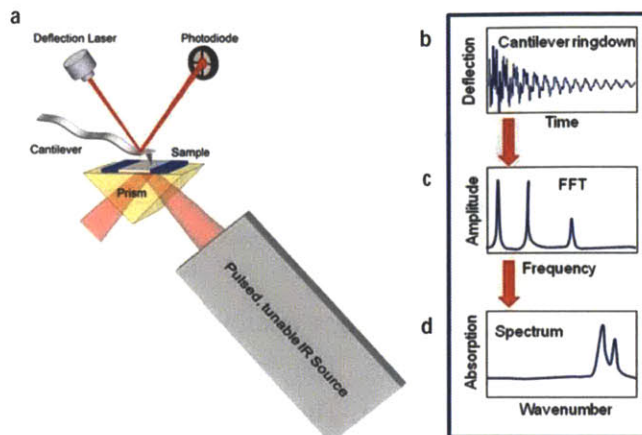


Figure 1-4 : Nano IR system using a tunable pulsed infrared source and an atomic force microscope tip. (a) A tunable pulsed infrared (IR) source from 2.5 μm to 10 μm heats up the sample. AFM tip detects the thickness variation of the sample due to the thermal expansion. The deflection laser is reflected off the back side of the cantilever to measure the deflection. (b) The deflection signal in time domain is recorded by the photodiode. (c) Fast Fourier Transform (FFT) of the signal in part (b), which provides the spectral information. (d) Change the x coordinate from modulated frequencies to wavenumber. Figures adapted from Ref. 21 and 22.

The Nano-FTIR system is a scattering-type scanning near-field optical microscopy consisting of a FTIR system and an AFM-cantilever (Fig. 1-5).²³ An AFM-tip serves to disturb local field such that the backscattered light signal from the metal tip of the AFM-cantilever is analyzed by the Fourier transform, and the scattered field from the oscillating metallic tip is analyzed with an asymmetric Fourier transform spectrometer. The spatial resolution is 20nm due to the same reason, the size of the AFM tip, as Nano IR system, and it also utilizes the broadband spectroscopy using the Michelson interferometer. The absorption spectra of the poly-(methyl methacrylate) and poly-(dimethyl siloxane) are measured by this system.²³

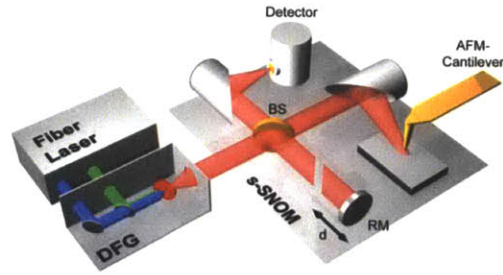


Figure 1-5 : Nano-FTIR using a Michelson interferometer and a scattering-type scanning near-field optical microscopy. Nano-FTIR uses an Er-fiber-laser system that emits a pulse train at $1.55 \mu\text{m}$ (blue) and a broadened and red-shifted laser (green). A difference frequency generator (DFG) unit superimposes both beams in a nonlinear crystal that emits a mid-infrared (MIR) continuum beam that illuminates the atomic force microscopy (AFM) tip. The intensity modulation is done by a beam splitter (BS) and a moving reference mirror (RM). It is a scattering-type scanning near-field optical microscopy (s-SNOM). Figures adapted from Ref.23.

To sum up, each micro/nano spectroscopy has its own advantages and limits. Existing micro/nano spectroscopy methods have been able to do qualitative broadband measurements and have the spatial resolution as small as 20 nanometers. It is difficult to carry out quantitative absorptance measurement due to limitations from sample size, placements, or sensitivity of the detectors. This thesis develops a new micro/nano spectroscopy method that can be applied directly to measure micro/nanoscale samples by combining a tipless bilayer cantilever and the FTIR system. The sample is placed on the cantilever (sample arm) that is thermally linked to the bilayer cantilever (detector arm). This configuration allows quantitative measurements of an isolated material and pattern structures through the power calibration.

1.4 Summary

With the quick development of nanotechnology, the micro/nano- spectroscopy is important to provide the optical properties that characterize micro and nanometer-sized structures. This thesis develops a new platform for micro/nano-spectroscopy, which includes the benefits described in Sections 1.1-1.2. This new method combines the Michelson interferometer as an input source and a cantilever as the sample stage and heat flux probe. Its benefits include broadband spectroscopy, direct and quantitative measurements, ultra-high sensitivity, and a isolated material or patterned structures characterization. In particular, the quantitative measurement and the single material and patterned structures characterization cannot be easily done by existing methods of micro/nano spectroscopy that are reviewed in Section 1.3.

In this thesis, the theoretical model and the experimental demonstration are shown. Chapter 2 gives the schematic and the theoretical model of this new method. Chapter 3 gives the steps of calibrations to measure quantitative data. Chapter 4 uses the Si/Al thin film cantilever as a demonstration of the direct and quantitative broadband absorptance spectroscopy. Chapter 5 provides a summary of our current work, an extension platform designed by Dr. Brian R. Burg et al., and the future directions.

Chapter 2

System and Operating Principle of the Direct and Quantitative Broadband Absorptance Micro/Nano Spectroscopy

Chapter 2 provides an outline and theoretical models to describe the system of the direct and quantitative broadband absorptance micro/nano-spectroscopy using FTIR and a bilayer cantilever probe. Section 2.1 shows the schematic of this new method, and the connection between each component. Section 2.2 describes the operating principle of Michelson interferometer, and the theoretical model that relates the modulated frequencies and the wavelengths of light. Section 2.3 discusses the fiber optics and the Gaussian profile that is used to fit the spatial intensity distribution. Section 2.4 derives the governing equation of the dynamic bilayer cantilever, and the frequency response solved by using the harmonic solution.

2.1 System

Our approach to measure spectral absorptance of micro/nanometer-sized object is based on thermally connecting micro/nano samples to a bilayer cantilever. The

bending of the bilayer cantilever is measured by excitation with broadband radiation generated by a conventional FTS. Fourier transform analysis of the bending signal is then used to extract the absorbance data.

In the proposed system, the modulated light from the Michelson interferometer is coupled into a polycrystalline infra-red (PIR) fiber via an optical fiber coupler (JT Ingram Technologies, Fibermate2™ FTIR Fiber Coupler) and is directed toward the sample. The sample is attached on a sample stage that is thermally linked to the bilayer cantilever probe. The system basically consists of a light source assembly and a probe and detector assembly. The light source assembly includes a broadband light source, an interferometer, an optical coupler, and an optical fiber. The probe and detector assembly combines the sample, a bilayer cantilever probe, a Position Sensitive Detector (PSD), and a computer to carry out Fourier transform analysis. Fig. 2-1 shows the general diagram and specific components used in the demonstration of this new method with subsequent results presented in Chapters 2, 3 and 4. The broadband light source of the Michelson interferometer dictates the spectral range of the absorption measurement and can conceivably cover any region, e.g. ranging from infrared to visible, or ultraviolet. The interferometer modulates the intensity of the broadband light source, providing a means of spectrally resolving electromagnetic radiation, and a detailed explanation is provided in Section 2.2. Except for the Michelson interferometer, different types of interferometers can be used including the Mach-Zender interferometer, Sagnac interferometer, Bath interferometer, or Fabry-Perot interferometer.

The bilayer cantilever is used as both the probe and the sample stage to measure the optical absorbance of the sample directly and quantitatively. Fig. 2-2 illustrates how the cantilever, made of two material layers with different coefficients of thermal expansion, behaves when light is absorbed. When the sample absorbs light,

the energy will conduct along the sample and the cantilever towards the base of the cantilever via heat conduction. This causes the temperature of the cantilever to rise, and the bilayer cantilever will bend. The deflection of the cantilever is then measured optically using a laser reflected off the cantilever onto a PSD. The cantilever deflection signal is ultimately analyzed using Fourier transform analysis to extract the absorption properties of the sample. To extract quantitative data, additional calibrations are needed as discussed in Chapter 3. The bilayer cantilever is the essential part to function as the principle thermal sensor in this system. The bilayer cantilever (the probe arm) is thermally linked to the sample holder (the sample arm), or can serve as the sample holder itself, as shown in Fig. 2-3(a) and Fig. 2-3(b).

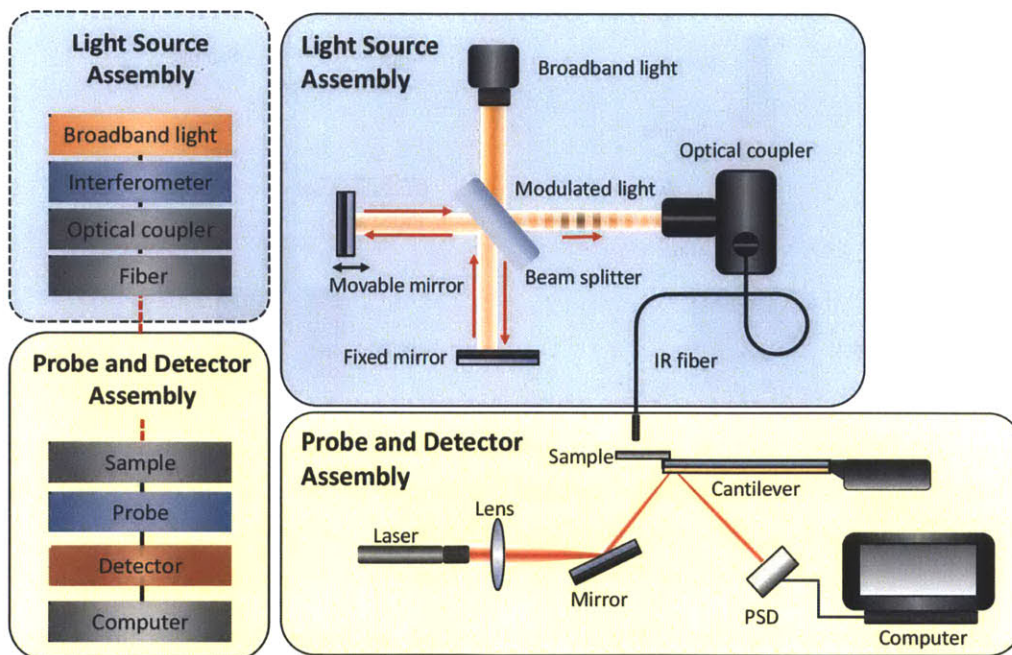


Figure 2-1 : Schematic of the system in this thesis combining a light source assembly and a detector and probe assembly. Left figure shows the general diagram of the system, and the right diagram shows the specific components. In the right diagram, the light source assembly combines a broadband light source, a Michelson interferometer, an optical coupler, and a polycrystalline infra-red (PIR) fiber. The modulated light is coupled into a PIR fiber using an optical coupler. The probe and detector assembly is made up of the sample placed on a bilayer cantilever probe,

which simultaneously acts the sample stage and heat flux probe. The deflection signal of the cantilever is measured by the Position Sensitive Detector (PSD) and the signal is post-processed using Fourier transform analysis by computer.

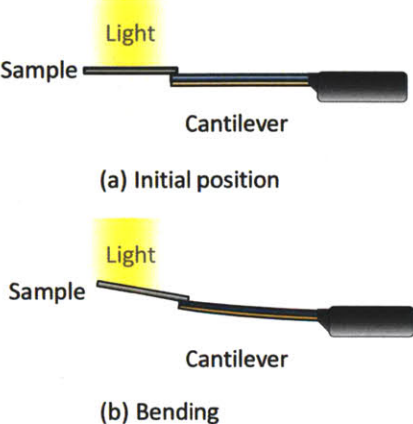


Figure 2-2 : Bending of a bilayer cantilever beam due to a temperature change. (a) Initial position of the cantilever before heating. (b) The bent position after heating.

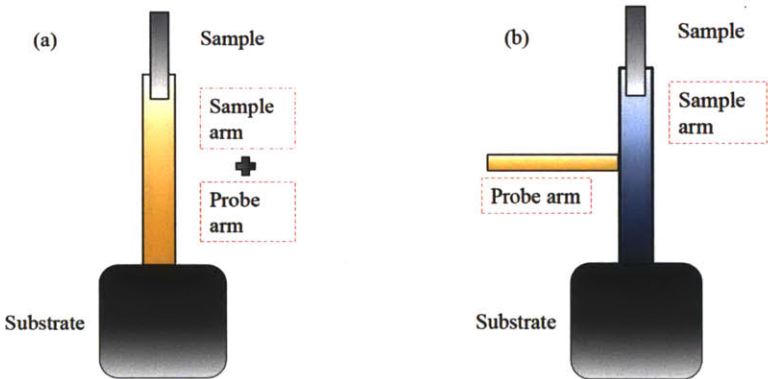


Figure 2-3 : Different sample and probe configurations of decoupled cantilever arms.²³ (a) The bilayer cantilever functions as both the sample holder and the probe. (b) The sample arm is separated from the probe arm (the bilayer cantilever).

To demonstrate the feasibility of the concept, an experimental set-up is built using a FTIR system with a Michelson interferometer, a polycrystalline infra-red (PIR) fiber, and a tipless silicon/aluminum bilayer cantilever. The following sections introduce the theory of the operating principle of each component. The Michelson interferometer, fiber optics, and dynamic behavior of a bilayer cantilever are presented in Sections 2.2, 2.3, and 2.4 respectively.

2.2 Michelson Interferometer

FTIR uses the Michelson interferometer to modulate the intensity of its broadband light source and the Fourier transform technique to distinguish the spectral behaviors, so the broadband measurement is feasible in a single scan. The FTIR system used is a PerkinElmer Spectrum GX, and its light source consists of a wire coil that operates at 1100K, covering the wavelength range from near-infrared ($2\mu\text{m}$) to mid-infrared ($\sim 25\mu\text{m}$).

Fig. 2-4 shows the schematic and the operating principle of the Michelson interferometer, and the operating principle as follows. When the light beam hits the beam splitter, half of the light is transmitted and the other half is reflected. The transmitted light is directed toward a fixed mirror, while the reflected light is directed towards a moveable mirror. The mirrors then reflect the two light beams back to the beam splitter resulting in interference. This interference is dependent on the difference in the optical path lengths of the two beams. If the distances from the beam splitter to the moveable mirror and the fixed mirror are equal (or integer multiples of a particular wavelength), the two beams constructively interfere. However, if the moveable mirror is shifted by half the wavelength, the two beams will destructively interfere. Therefore, as this mirror is continually moved, it will transit between points of constructive and destructive interference.

(a) Michelson Interferometer

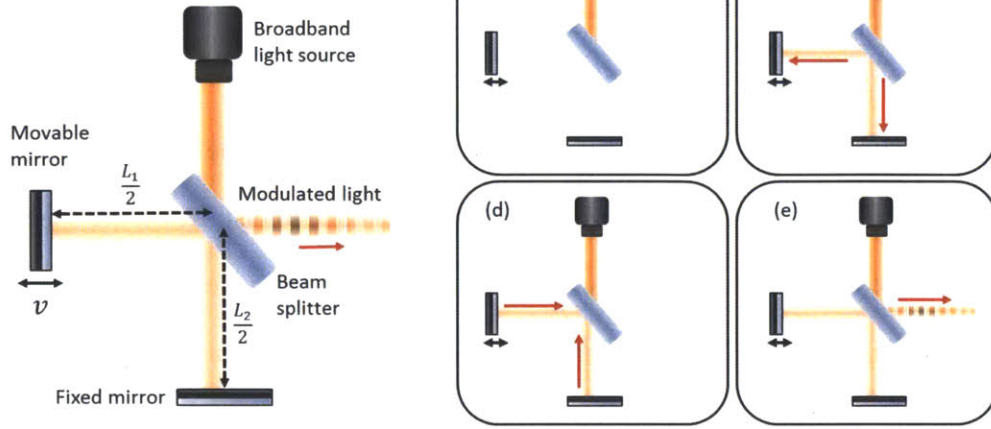


Figure 2-4 : Operating principle of the Michelson interferometer. Figure (a) indicates each component, and figures (b) to (e) show the operating steps. Broadband light separates into two beams after transmitting the beam splitter, and two beams are reflected back from the movable and fixed mirrors respectively. When they meet each other, the interference causes the modulated light.

In a theoretical model, the two light paths can be assumed to have the same amplitude, and expressed as ²⁴

$$\psi_{fixed} = \psi_0 e^{i(2\pi f_{IR})t} \quad \text{and} \quad \psi_{movable} = \psi_0 e^{i(2\pi f_{IR}t + \phi)} \quad (3)$$

where ψ_{fixed} is the source wave reflected from the fixed mirror, $\psi_{movable}$ is the source wave reflected from the movable mirror, ψ_0 is the amplitude, f_{IR} is the frequency of light at one specific wavelength, and ϕ is the phase difference due to the movable mirror. When two beams meet each other at the beam splitter, the interference wave can be written as

$$\begin{aligned} \psi_{interference} &= \psi_{fixed} + \psi_{movable} \\ &= \psi_0 e^{i(2\pi f_{IR})t} + \psi_0 e^{i(2\pi f_{IR}t + \phi)} \end{aligned} \quad (4)$$

Its intensity is the square of the wave function, so it is expressed as

$$\begin{aligned}
I_{interference} &= |\psi_{interference}|^2 \\
&= |\psi_0 e^{i(2\pi f_{IR})t} + \psi_0 e^{i(2\pi f_{IR}t + \phi)}|^2 \\
&= |\psi_0 e^{i(2\pi f_{IR})t} \cdot (1 + e^{i\phi})|^2 \quad (5) \\
&= |\psi_0 e^{i(2\pi f_{IR})t} \cdot (1 + \cos(\phi) + i\sin(\phi))|^2 \\
&= |\psi_0|^2 |e^{i(2\pi f_{IR})t}|^2 |2 + 2\cos(\phi)| \\
&= 2\psi_0^2 \cdot [1 + \cos(\phi)]
\end{aligned}$$

where the phase difference between the two waves is related to the optical path difference (OPD) of L_1 and L_2 in Fig. 2-4,

$$\frac{\phi}{2\pi} = \frac{OPD}{\lambda_{IR}} \rightarrow \phi = \frac{2\pi \cdot OPD}{\lambda_{IR}} = 2\pi \cdot \frac{2v}{\lambda_{IR}} \cdot t = 2\pi \cdot f \cdot t \quad (6)$$

λ_{IR} is one specific wavelength from the broadband light source. $\frac{L_1}{2}$ and $\frac{L_2}{2}$ are the distance between the beam splitter to the movable mirror and the fixed mirror respectively. The factor of 2 is due to the round trip of optical path length. f is the modulated frequency of intensity. The intensity of each wavelength, λ , or wavenumber, $\eta = \frac{1}{\lambda}$, is modulated by a specific frequency, f , dependent on the velocity of the moveable mirror, v . The mirror motion and the modulated periodic frequency with respect to its corresponding wavelength follow the relation:

$$f = \frac{2v}{\lambda_{IR}} = 2v\eta_{IR} \quad (7)$$

The intensity of a broadband light source modulated by the Michelson interferometer is a integration of equation (5) for all wavelengths :

$$I_{broadband}(t) = \int 2\psi_i^2 \cdot [1 + \cos(2\pi \cdot f_i \cdot t)]df \quad (8)$$

The resulting modulated light of equation (8) forms an interferogram pattern. Fig. 2-5 simulates an interferogram pattern using a movable mirror velocity of $2v = 0.06[\frac{cm}{s}]$ and a blackbody at 1100K, and the wavelength cutoff is between $1\mu m$ and $20\mu m$. Note that the velocity of mirror can change the modulated frequencies to get a different inteferogram.

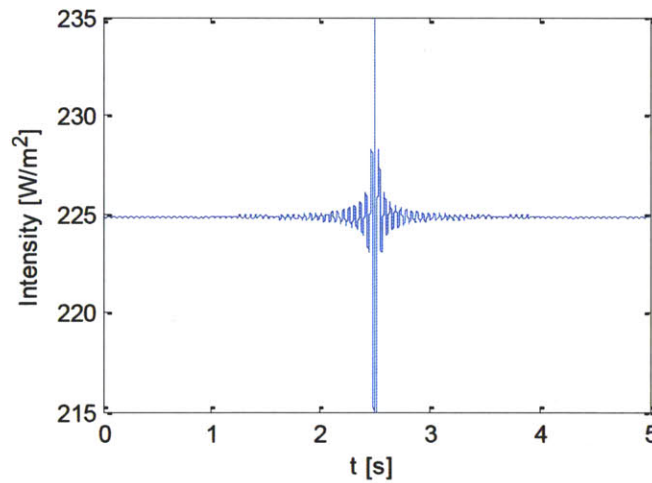


Figure 2-5 : A simulated interferogram pattern from a Michelson interferometer. The light is modulated in time using a moving mirror velocity of $2v = 0.06[\frac{cm}{s}]$. The diagram is simulated for a blackbody at 1100K, and the wavelength cutoff is between $1\mu m$ and $20\mu m$.

2.3 Fiber Optics

To have sufficient power, a fiber is easy to concentrate light on the sample, and it can also direct light into a vacuum chamber for reduction of convective loss and a stable environment.

Light propagating in the fiber is based on total internal reflection.^{25,26,27} According to Snell's law, total reflection happens when light is incident from a material with higher refractive index to a material with lower refractive index. Its critical angle is

$$\theta_{cr} = \sin^{-1}\left(\frac{n_2}{n_1}\right) \quad (9)$$

where n_1 is the refractive index of material 1, and n_2 is the refractive index of material 2. In Fig. 2-6, when the incident angle, θ_1 , is larger than the critical angle, the light can propagate in the fiber.

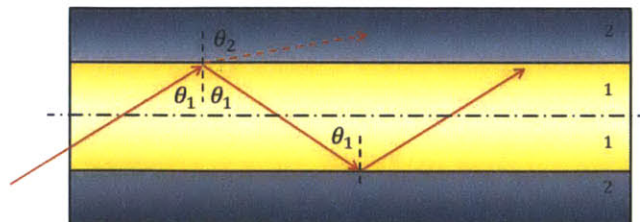


Figure 2-6 : Operating principle of the fiber. According to Snell's law, total reflection happens when light is incident from the core (material 1) with a higher refractive index to the clad (material 2) with a lower refractive index. θ_1 is the incident angle,

and θ_2 is the refractive angle.

Our system uses an optical coupler (JT Ingram Technologies, Fibermate2™ FTIR Fiber Coupler) to concentrate the broadband light into the polycrystalline infra-red (PIR) fiber. Four effects are needed to be noticed as follow. First, only the cross-sectional area of the core accepts the incoming light, so the concentrating light outside the cross-section of the core region will be neglected. Second, transmission of light by the fiber is not lossless. There are several reasons causing the loss including absorption from the core and cladding and leakage from the cladding. Fig. 2-7 is the transmission spectrum of a 4-meters long PIR fiber from Advanced Research & Technology in Photonics. Its peak value is around $11.1\mu\text{m}$ (900cm^{-1}), and $>10\%$ transmission happens to be from $4.3\sim 16.7\mu\text{m}$ ($2300\sim 600\text{cm}^{-1}$). Third, light from the fiber has a divergent angle, $\theta_{divergent}$ and it depends on the materials of the core and cladding. Numerical Aperture (NA) is used to express the divergent angle:²⁸

$$NA = n \cdot \sin\theta_{divergent} = \sqrt{n_1^2 - n_2^2} \quad (10)$$

where n is the refractive index of the environmental material, which is air ($n=1$) in our case. Fourth, Gaussian distribution function is often used to fit the intensity distribution from the fiber.^{29,30} The Gaussian function is

$$f(x; \mu, \sigma^2) = \frac{1}{\sigma\sqrt{2\pi}} e^{-\frac{1}{2}\left(\frac{x-\mu}{\sigma}\right)^2} \quad (11)$$

where μ and σ are the mean and the standard deviation respectively. These two parameters can be used to fit the intensity distribution. Fig. 2-8 shows the intensity of

the PIR fiber, and it is recorded by the IR camera (FLIR system, Inc. ExaminIR™).

Along the y pixels, the maximum curve (8th row of the x pixel) is fitted by the Gaussian function with $\mu = 0$ and $\sigma^2 = 0.83$, and the results are shown in Fig. 2-9.

To find out a suitable value of σ , the method of least squares of errors is applied. Fig.

2-10 shows the least squares of errors is happened to $\sigma^2 = 0.83$.

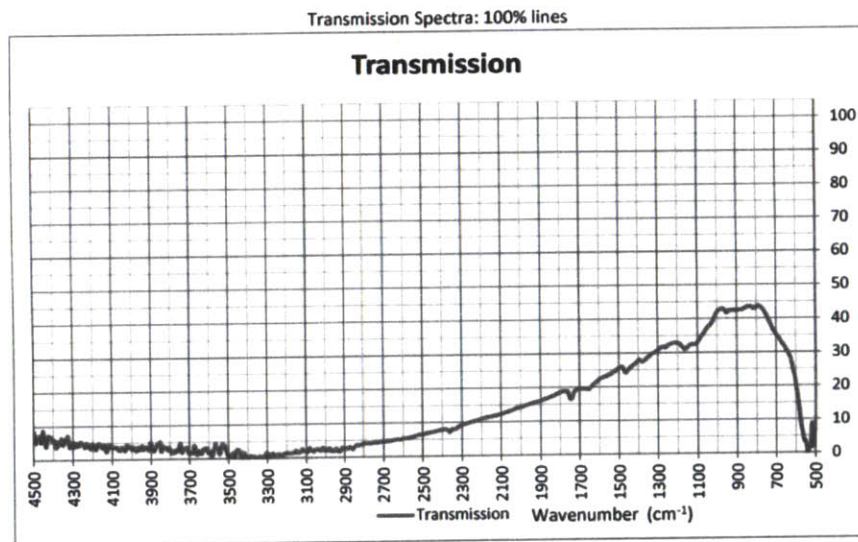


Figure 2-7 : Transmission of the polycrystalline infra-red (PIR) fiber. This spectrum is provided from Advanced Research & Technology in Photonics. The peak value is around $11.1\mu\text{m}$ (900cm^{-1}), and $>10\%$ transmission happens to be from $4.3\sim 16.7\mu\text{m}$ ($2300\sim 600\text{cm}^{-1}$).

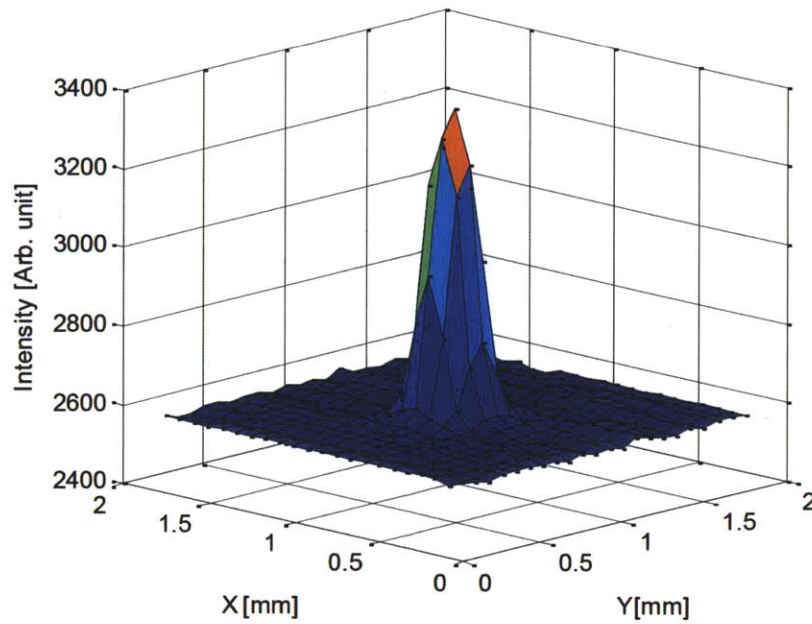


Figure 2-8 : Intensity of the polycrystalline infra-red fiber. These data are recorded by the IR camera (FLIR system, Inc. ExaminIR™).

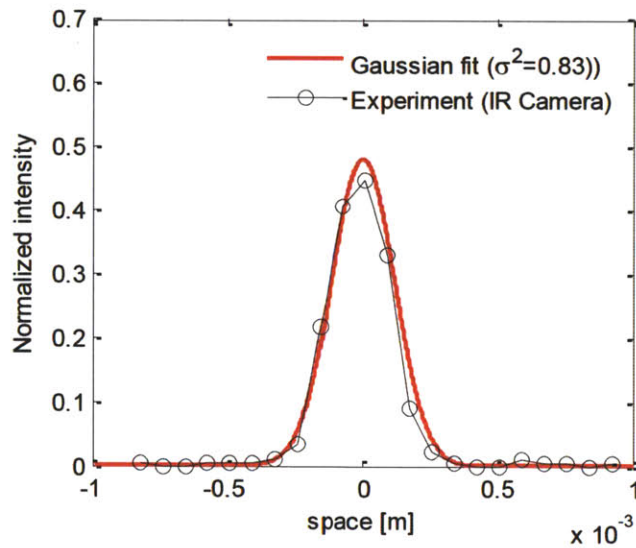


Figure 2-9 : Gaussian function fitting of the intensity distribution of the polycrystalline infra-red fiber. $\mu = 0$ and $\sigma^2 = 0.83$ are chosen to fit the data recorded by the IR camera.

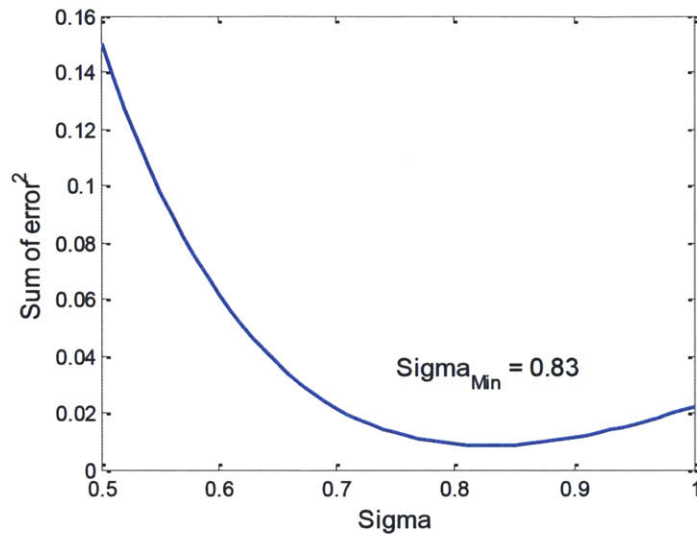


Figure 2-10 : Least squares method fitting for the standard deviation of σ of the Gaussian function. The method is applied to find out the σ of minimum summation of squares of errors is 0.83.

2.4 Dynamic Behavior of the Bilayer Cantilever

Dynamic measurements offer advantages including avoiding noise and broadband measurement. Lock-in amplifiers are often used as a band-pass filter to track the amplitude at a specific frequency for reduction of noise.^{1,8,10,11,31} fast Fourier transform provides the spectral analysis of dynamic measurement. In the system of Fig. 2-1, Michelson interferometer supplies a dynamic input, so it is necessary to understand the dynamic behavior of the bilayer cantilever. In this thesis, the fast Fourier transform is used to study the broadband absorptance spectra of samples instead of using the lock-in amplifier.

2.4.1 Frequency Response of Temperature

Temperature distribution along the length direction controls the deflection of the

bilayer cantilever. Since the thickness is much smaller than the length, temperature is assumed to be constant along the thickness direction. Therefore, one dimensional fin model is used to estimate the temperature.³² Fig. 2-11 shows the coordinate and the differential element of the bilayer cantilever for a uniform heating case. From the energy conservation, the increase of temperature of the differential element is equal to the difference of the input heat flux and the output heat flux:

$$\begin{aligned}
w(\rho_1 c_1 t_1 + \rho_2 c_2 t_2) \cdot dx \frac{\partial}{\partial t} [T_{(x,t)}] &= \dot{Q}_{in} - \dot{Q}_{out} \\
= -w(k_1 t_1 + k_2 t_2) \frac{\partial}{\partial x} [T_{(x,t)}] + \dot{q}_{(t)} w \cdot dx & \\
- \left\{ -w(k_1 t_1 + k_2 t_2) \frac{\partial}{\partial x} [T_{(x+dx,t)}] \right\} & \\
-h \cdot 2(t_1 + t_2 + w) \cdot dx \cdot [T_{(x,t)} - T_o] &
\end{aligned} \tag{12}$$

The equation (12) can be simplified by Taylor's expansion to the first order:

$$\begin{aligned}
\frac{\partial}{\partial t} [T_{(x,t)}] &= \frac{\dot{q}_{(t)}}{(\rho_1 c_1 t_1 + \rho_2 c_2 t_2)} + \frac{(k_1 t_1 + k_2 t_2)}{(\rho_1 c_1 t_1 + \rho_2 c_2 t_2)} \frac{\partial^2}{\partial x^2} [T_{(x+dx,t)}] \\
&\quad - \frac{h \cdot 2(t_1 + t_2 + w)}{w(\rho_1 c_1 t_1 + \rho_2 c_2 t_2)} \cdot [T_{(x,t)} - T_o]
\end{aligned} \tag{13}$$

where $\rho_1 \left[\frac{kg}{m^3} \right]$, $c_1 \left[\frac{J}{kg \cdot K} \right]$, and $t_1 [m]$ are the density, specific heat, thickness of material 1, ρ_2 , c_2 , and t_2 are the density, specific heat, thickness of material 2, w is the width of the cantilever, $T_{(x,t)}$ is the temperature of the bilayer cantilever, T_o is the environmental temperature, h is the convection coefficient, and $\dot{q}_{(t)} \left[\frac{W}{m^2} \right]$ is the absorbed power per area. For convenience, equation (13) is rewritten as

$$\frac{\partial}{\partial t} [T_{(x,t)}] = a_1 \frac{\partial^2}{\partial x^2} [T_{(x+dx,t)}] + a_2 \cdot [T_{(x,t)} - T_o] + a_3 \tag{14}$$

where $a_1 = \frac{(k_1 t_1 + k_2 t_2)}{(\rho_1 c_1 t_1 + \rho_2 c_2 t_2)}$, $a_2 = -\frac{h \cdot 2(t_1 + t_2 + w)}{w(\rho_1 c_1 t_1 + \rho_2 c_2 t_2)}$, and $a_3 = \frac{q(t)}{(\rho_1 c_1 t_1 + \rho_2 c_2 t_2)}$.

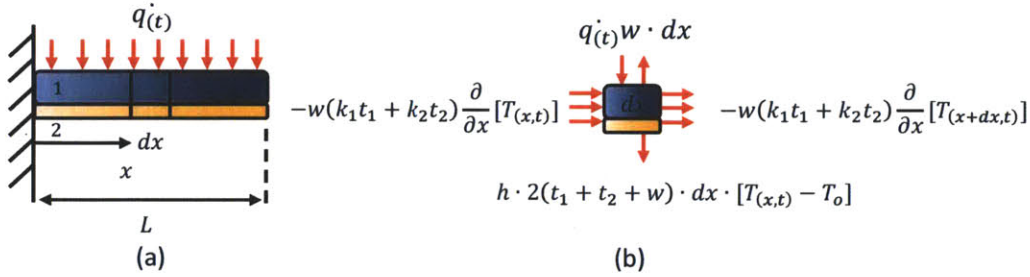


Figure 2-11 : Schematic of the coordinate system and the differential element of the uniformly heating. (a)The coordinate system. (b)Energy balance of a differential element of the fin model.

To find out the frequency response of temperature in the cantilever, the heating input is assumed to be a harmonic excitation. Assume $q(t) = \beta(\omega)e^{i\omega t}$ and $T(x,t) - T_o = \tau(x)e^{i\omega t}$, where $\beta(\omega)$ and $\tau(x)$ are amplitudes of the absorbed power and temperature respectively, and equation (14) becomes

$$i\omega\tau(x) = a_1 \frac{\partial^2}{\partial x^2} [\tau(x)] + a_2 \cdot [\tau(x)] + a_3 \quad (15)$$

Let $\tau_h(x) = e^{\lambda x}$ to find out the eigenvalues of equation (15):

$$i\omega = a_1 \lambda^2 + a_2 \rightarrow \lambda = \pm \sqrt{\frac{i\omega - a_2}{a_1}} \quad (16)$$

Let $\tau_p(x) = c_3$ to find out the particular solution of equation (15):

$$c_3 = -\frac{a_3}{a_2 - i\omega} \quad (17)$$

The general solution is

$$\tau_{(x)} = \tau_{h(x)} + \tau_{p(x)} = c_1 e^{\lambda x} + c_2 e^{-\lambda x} + c_3 \quad (18)$$

Now, apply the boundary conditions at the fixed end and the free end to equation (18). Due to the assumption of perfect heat sink at the fixed end, the temperature is at room temperature. The cross-sectional area of the tip at the free end is much smaller than the area of the sides, so the adiabatic boundary condition applies to the free end. The mathematical expressions of the two boundary conditions are

$$\tau_{(x=0)} = 0 \quad \text{and} \quad \frac{\partial}{\partial x} [\tau_{(x=L)}] = 0 \quad (19)$$

For $\frac{\partial}{\partial x} [\tau_{(x=L)}] = 0$,

$$c_2 = -\frac{c_3}{1 + e^{-2\lambda L}} \quad (20)$$

For $\tau_{(x=0)} = 0$,

$$c_1 = c_2 e^{-2\lambda L} \quad (21)$$

Table 1. The thermal and dimensional properties of the silicon/aluminum cantilever.

	Silicon(Si) ^{8,10}	Aluminum(Al) ^{8,10,33}
Thermal conductivity, $k \left[\frac{W}{m \cdot K} \right]$.	150	237
Density, $\rho \left[\frac{kg}{m^3} \right]$	2328	2702

Specific heat, $c \left[\frac{J}{kg \cdot K} \right]$	700	908
Thickness*, $t [nm]$	800 (500-2500)**	250
Total length*, $L [\mu m]$	500	
Width*, $w [\mu m]$	100	
Convection coefficient, ¹⁴ $h \left[\frac{W}{m^2 \cdot K} \right]$	3400	
Total power input, $q_{(t)} w L [\mu W]$ (Uniformly heating)	1	
Total power input, $q_{(t)} w (t_1 + t_2) [\mu W]$ (Tip heating)	1	

* Physical vapor deposition (PVD) is used to deposit an aluminum layer of 250 nm onto the commercially available silicon cantilever (Nanoworld, Arrow TL1).

** The thickness of the silicon layer varies from 500 to 2500nm provided by NanoWorld.

Fig. 2-13 shows the frequency response of temperature at the tip ($x = 500 \mu m$) with the uniformly heating by using Table 1. Considering the total power of $1 \mu W$, the maximum amplitude of the temperature approaches 2.6mK at low frequencies, and it decreases with increasing driving frequency. Higher driving frequency reduces the amplitude of temperature because of the phase delay of the thermal diffusive velocity.

Fig. 2-12 shows the coordinate and the differential element of the bilayer cantilever for a tip heating case. Similarly, using the energy conservation, the thermal diffusion equation is

$$\frac{\partial}{\partial t} [T_{(x,t)}] = a_1 \frac{\partial^2}{\partial x^2} [T_{(x+dx,t)}] + a_2 \cdot [T_{(x,t)} - T_o] \quad (22)$$

where its general solution is

$$\tau(x) = \tau_{h(x)} = c_1 e^{\lambda x} + c_2 e^{-\lambda x} \quad (23)$$

For the tip heating case, the boundary condition at the free end becomes the heating input, so the boundary conditions are

$$\tau_{(x=0)} = 0 \quad \text{and} \quad \frac{\partial}{\partial x} [\tau_{(x=L)}] = \frac{q(\dot{t})}{w(k_1 t_1 + k_2 t_2)} \quad (24)$$

For $\tau_{(x=0)} = 0$,

$$c_1 = c_2 \quad (25)$$

For $\frac{\partial}{\partial x} [\tau_{(x=L)}] = \frac{q(\dot{t})}{w(k_1 t_1 + k_2 t_2)}$,

$$c_1 = - \frac{q(\dot{t})}{w(k_1 t_1 + k_2 t_2) \cdot \lambda (e^{\lambda L} + e^{-\lambda L})} \quad (26)$$

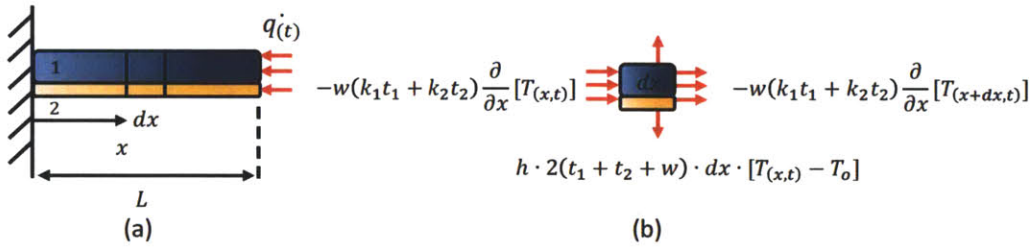


Figure 2-12 : Schematic of the coordinate system and the differential element of the tip heating. (a)The coordinate system. (b)Energy balance of a differential element of the fin model.

Similarly, Fig. 2-13 also shows the frequency response of temperature at the tip ($x = 500 \mu m$) with the tip heating by using the same Table 1. With the same total power of $1 \mu W$, the amplitude of the temperature is 9mK at 0Hz, and it also decreases with increasing driving frequency. Compare with the uniform heating case,

the temperature amplitude of the tip heating case is about 3.5 times higher than the value of the uniform heating case.

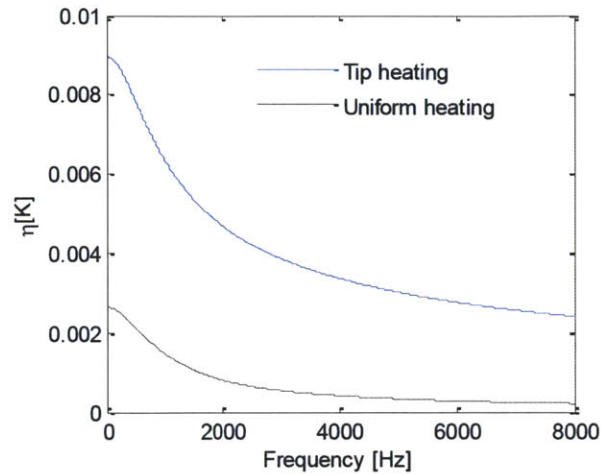


Figure 2-13 : Frequency response of temperature of the Si/Al bilayer cantilever with total power of $1 \mu W$. The temperature amplitude of the tip heating case is about 3.5 times higher than the value of the uniform heating case.

2.4.2 Frequency Response of Deflection

The frequency response of the cantilever temperature can be used to estimate the amplitude of deflection at a given driving frequency. Time-dependent deflection equation is required to solve the frequency response of deflection of the bilayer cantilever. Free body diagram is used to derive the governing equation.^{7,34} Fig. 2-14 shows the coordinate system and the free body diagram of the bilayer cantilever. Assume $\alpha_2 > \alpha_1$, and $\alpha_1 [K^{-1}]$ and $\alpha_2 [K^{-1}]$ are the thermal expansion coefficient of material 1 and 2 respectively. Four equations are required to derive the governing equation. First, the force balance along x axis is

$$P_1 + P_2 + \frac{\partial P_2}{\partial x} dx - P_2 - P_1 + \frac{\partial P_1}{\partial x} dx = 0 \quad (27)$$

which implies

$$\frac{\partial P_1}{\partial x} = \frac{\partial P_2}{\partial x} \rightarrow P_1 = P_2 = P \quad (28)$$

Because the boundary conditions of force are $P_{1(x=L)} = 0$ and $P_{2(x=L)} = 0$. P_1 and P_2 are the normal force on the material 1 and 2 respectively. Since P_1 is equal to P_2 , it is simply to express the normal force as $P_1 = P_2 = P [N]$. Second, the strain balance at the interface of material 1 and 2 is

$$\alpha_2 (T_{(x,t)} - T_o) - \frac{P_2}{E_2 w t_2} - \frac{t_2}{2r} = \alpha_1 (T_{(x,t)} - T_o) + \frac{P_1}{E_1 w t_1} + \frac{t_1}{2r} \quad (29)$$

where r is the curvature of the cantilever, E_1 and E_2 are the Young's modulus of material 1 and 2 respectively, and the equation (29) can be re-expressed as

$$P = \frac{(\alpha_2 - \alpha_1)(T_{(x,t)} - T_o) - \frac{t_1 + t_2}{2r}}{\frac{1}{E_1 w t_1} + \frac{1}{E_2 w t_2}} \quad (30)$$

Third, the moment balance is

$$\begin{aligned} M_2 + \frac{\partial M_2}{\partial x} dx + M_1 + \frac{\partial M_1}{\partial x} dx - M_1 - M_2 + \left[P + \frac{\partial P}{\partial x} dx \right] \frac{t_1 + t_2}{2} \\ - P \frac{t_1 + t_2}{2} + \left[V + \frac{\partial V}{\partial x} dx \right] dx = 0 \end{aligned} \quad (31)$$

where the $V[N]$ is the shearing force, and $M_1[N \cdot m]$ and $M_2[N \cdot m]$ are the moment of the materials 1 and 2 respectively. Equation (31) can be re-derived as

$$V = - \left[\frac{\partial M_1}{\partial x} + \frac{\partial M_2}{\partial x} - \frac{t_1 + t_2}{2} \frac{\partial P}{\partial x} \right] \quad (32)$$

Forth, apply Newton's second law to analyze the force along y axis:

$$V - \left(V + \frac{\partial V}{\partial x} dx \right) - C w dx \frac{\partial y}{\partial t} = w(\rho_1 t_1 + \rho_2 t_2) dx \frac{\partial^2 y}{\partial t^2} \quad (33)$$

which is

$$- \frac{\partial V}{\partial x} = w(\rho_1 t_1 + \rho_2 t_2) \frac{\partial^2 y}{\partial t^2} + C \frac{\partial y}{\partial t} \quad (34)$$

where y is not only a coordinate, but it stands for the deflection of the bilayer cantilever, and $C \left[\frac{N \cdot s}{m^2} \right]$ is the damping coefficient. Apply equation (30), (32),

$$M_1 = \frac{E_1 I_1}{r}, \quad M_2 = \frac{E_2 I_2}{r}, \quad I_1 = \frac{w t_1^3}{12}, \quad I_2 = \frac{w t_2^3}{12} \text{ and } \frac{1}{r} = \frac{\frac{\partial^2 y}{\partial x^2}}{[1 + (\frac{\partial y}{\partial x})^2]^{\frac{3}{2}}} \approx \frac{\partial^2 y}{\partial x^2} \text{ when}$$

$\frac{\partial y}{\partial x} \ll 1$ to equation (34):

$$\frac{\partial}{\partial x} \left[\frac{\partial}{\partial x} \left(\frac{E_1 I_1}{r} \right) + \frac{\partial}{\partial x} \left(\frac{E_2 I_2}{r} \right) - \frac{t_1 + t_2}{2} \frac{\partial}{\partial x} \left(\frac{(\alpha_2 - \alpha_1)(T_{(x,t)} - T_o) - \frac{t_1 + t_2}{2r}}{\frac{1}{E_1 w t_1} + \frac{1}{E_2 w t_2}} \right) \right] = w(\rho_1 t_1 + \rho_2 t_2) \frac{\partial^2 y}{\partial t^2} + C \frac{\partial y}{\partial t}$$

$$\rightarrow \left[(E_1 I_1 + E_2 I_2) - \frac{(t_1 + t_2)^2}{\frac{1}{E_1 w t_1} + \frac{1}{E_2 w t_2}} \right] \frac{\partial^4 y}{\partial x^4} + w(\rho_1 t_1 + \rho_2 t_2) \frac{\partial^2 y}{\partial t^2} + c \frac{\partial y}{\partial t} = - \frac{(\alpha_2 - \alpha_1) \frac{t_1 + t_2}{2}}{\frac{1}{E_1 w t_1} + \frac{1}{E_2 w t_2}} \frac{\partial^2 T}{\partial x^2}$$

$$\rightarrow A \frac{\partial^4 y_{(x,t)}}{\partial x^4} + B \frac{\partial^2 y_{(x,t)}}{\partial t^2} + C \frac{\partial y_{(x,t)}}{\partial t} = E \frac{\partial^2 T_{(x,t)}}{\partial x^2} \quad (35)$$

where I_1 and I_2 are the second moments of inertia of materials 1 and 2, and

$$A = (E_1 I_1 + E_2 I_2) - \frac{(t_1 + t_2)^2}{\frac{1}{E_1 w t_1} + \frac{1}{E_2 w t_2}}$$

$$B = w(\rho_1 t_1 + \rho_2 t_2)$$

$$E = - \frac{(\alpha_2 - \alpha_1) \frac{t_1 + t_2}{2}}{\frac{1}{E_1 w t_1} + \frac{1}{E_2 w t_2}}$$

Equation (35) is the governing equation of deflection of the bilayer cantilever.

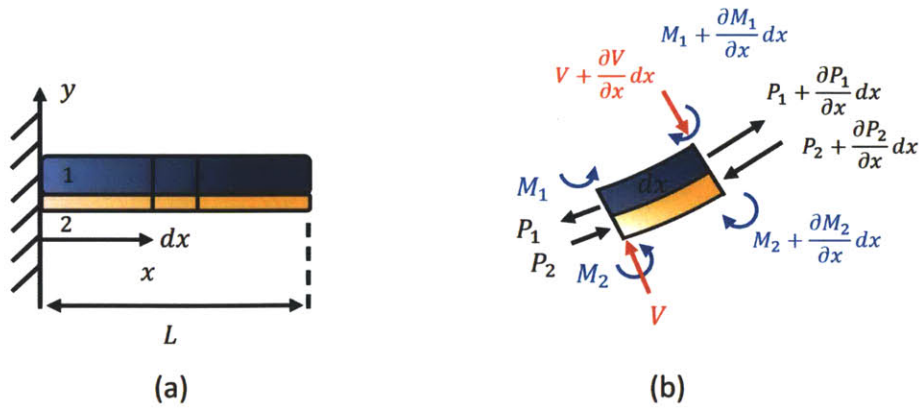


Figure 2-14 : Schematic of the coordinate system and the free body diagram of the bilayer cantilever. (a)Coordinate system. (b)Free body diagram of a differential element.

Similarly, to find out the frequency response of deflection, the temperature is

assumed to be a harmonic excitation. Assume $y_{(x,t)} = \xi_{(x)}e^{i\omega t}$ and $T_{(x,t)} - T_o = \tau_{(x)}e^{i\omega t}$, and equation (35) becomes

$$A \frac{\partial^4 \xi_{(x)}}{\partial x^4} - B\omega^2 \xi_{(x)} + iC\omega \xi_{(x)} = E \frac{\partial^2 \tau_{(x)}}{\partial x^2} \quad (36)$$

Apply equation (18) or (23) to equation (36) depending on the case of uniform heating or tip heating:

$$A \frac{\partial^4 \xi_{(x)}}{\partial x^4} - B\omega^2 \xi_{(x)} + iC\omega \xi_{(x)} = E [c_1 \lambda^2 e^{\lambda x} + c_2 \lambda^2 e^{-\lambda x}] \quad (37)$$

Let $\xi_{h(x)} = e^{Fx}$ to find out the eigenvalues of equation(37):

$$AF^4 - B\omega^2 + iC\omega = 0 \rightarrow F = \pm \left(\frac{B\omega^2 - iC\omega}{A} \right)^{\frac{1}{4}} \text{ or } \pm i \left(\frac{B\omega^2 - iC\omega}{A} \right)^{\frac{1}{4}} \quad (38)$$

Let $\xi_{p1(x)} = c_8 e^{\lambda x}$ and $\xi_{p2(x)} = c_9 e^{\lambda x}$, where c_8 and c_9 are coefficients, to find the particular solutions of equation(37):

$$c_8 (A\lambda^4 - B\omega^2 + iC\omega) = EC_1 \lambda^2 \rightarrow c_8 = \frac{EC_1 \lambda^2}{A\lambda^4 - B\omega^2 + iC\omega} \quad (39)$$

$$c_9 (A\lambda^4 - B\omega^2 + iC\omega) = EC_2 \lambda^2 \rightarrow c_9 = \frac{EC_2 \lambda^2}{A\lambda^4 - B\omega^2 + iC\omega} \quad (40)$$

Therefore, the solution of the harmonic excitation of equation (36) is

$$\xi_{(x)} = c_4 e^{Fx} + c_5 e^{-Fx} + c_6 e^{iFx} + c_7 e^{-iFx} + c_8 e^{\lambda x} + c_9 e^{\lambda x} \quad (41)$$

where c_4 , c_5 , c_6 , and c_7 are coefficients that are determined by the boundary conditions. The boundary conditions determine the behavior of the cantilever. For a cantilever, the boundary conditions at fixed end ($x=0$) and at free end ($x=L$) are³⁵

$$\xi_{(x=0)} = 0 \quad (42)$$

$$\frac{\partial \xi_{(x=0)}}{\partial x} = 0 \quad (43)$$

$$\frac{\partial^2 \xi_{(x=L)}}{\partial x^2} = 0 \quad (44)$$

$$\frac{\partial^3 \xi_{(x=L)}}{\partial x^3} = 0 \quad (45)$$

Equation (42) and (43) mean the deflection and slop at the fixed end are zero, and equation (44) and (45) implies there is no moment and shear stress at the free end. Apply the four boundary conditions of equation (42) - (45) to the equation (41):

$$\xi_{(x=0)} = 0 \rightarrow c_4 + c_5 + c_6 + c_7 + c_8 + c_9 = 0 \quad (46)$$

$$\frac{\partial \xi_{(x=0)}}{\partial x} = 0 \rightarrow c_4 F - c_5 F + i c_6 F - i c_7 F + c_8 \lambda - c_9 \lambda = 0 \quad (47)$$

$$\begin{aligned} \frac{\partial^2 \xi_{(x=L)}}{\partial x^2} = 0 \rightarrow c_4 F^2 e^{FL} + c_5 F^2 e^{-FL} - c_6 F^2 e^{iFL} - c_7 F^2 e^{-iFL} \\ + c_8 \lambda^2 e^{FL} + c_9 \lambda^2 e^{-FL} = 0 \end{aligned} \quad (48)$$

$$\frac{\partial^3 \xi_{(x=L)}}{\partial x^3} = 0 \rightarrow c_4 F^3 e^{FL} - c_5 F^3 e^{-FL} - i c_6 F^3 e^{iFL} + i c_7 F^3 e^{-iFL} + c_8 \lambda^3 e^{FL} - c_9 \lambda^3 e^{-FL} = 0 \quad (49)$$

Equation(46)-(49) can be written as a matrix:

$$\begin{bmatrix} 1 & 1 & 1 & 1 \\ F & -F & iF & -iF \\ F^2 e^{FL} & F^2 e^{-FL} & -F^2 e^{iFL} & -F^2 e^{-iFL} \\ F^3 e^{FL} & -F^3 e^{-FL} & -iF^3 e^{iFL} & iF^3 e^{-iFL} \end{bmatrix} \begin{bmatrix} c_4 \\ c_5 \\ c_6 \\ c_7 \end{bmatrix} = \begin{bmatrix} -c_8 - c_9 \\ -c_8 \lambda + c_9 \lambda \\ -c_8 \lambda^2 e^{\lambda L} - c_9 \lambda^2 e^{-\lambda L} \\ -c_8 \lambda^3 e^{\lambda L} + c_9 \lambda^3 e^{-\lambda L} \end{bmatrix} \quad (50)$$

Solving the matrix equations gives the coefficients of c_4 , c_5 , c_6 , and c_7 .

2.4.3 Three Fitted Properties

Before showing the frequency response results of deflection, mechanical properties are required. From literatures, the properties of silicon and aluminum are listed in the Table 1 and Table 2, and only the Young's modulus of thin films varies significantly. Since it is very difficult to fix one of the Young's modulus, an effective Young's modulus, $E_{effective}$, of the thermal drive is defined as

$$A = E_{effective}(I_1 + I_2) = (E_1 I_1 + E_2 I_2) - \frac{\frac{(t_1 + t_2)^2}{4}}{\frac{1}{E_1 w t_1} + \frac{1}{E_2 w t_2}} \quad (51)$$

Besides the Young's modulus, the convective heat transfer coefficient, h , and the damping coefficient, c , are unknown. These three parameters can be used to fit the experimental data to find out the properties of a bilayer cantilever

Table 2. The mechanical properties of the silicon/aluminum cantilever.

	Silicon(Si) ^{8,10,36,37,38}	Aluminum(Al) ^{8,10,39,40}
Young's modulus, $E[GPa]$.	62-169	47-70
Thermal expansion coefficient, $\alpha \left[\frac{1}{K} \right]$	2328	2702

Fig. 2-15 to Fig. 2-17 show the deflection frequency responses of the bilayer cantilever with uniform heating. These figures plot the amplitudes of deflection with different driving frequencies, and, generally, the amplitudes are reduced due to the phase delay of thermal diffusion; however, the amplitudes increase around their resonant frequencies. Fig. 2-15 plots the frequency response of deflection with different effective Young's modulus. Since the effective Young's modulus is attributed to the resonant frequency, the resonant frequency can fit the property of the Young's modulus first. Fig. 2-16 calculates the responses with different damping coefficients. The damping coefficient determines the peak and width of the resonant frequency, so the shape of the response at the resonant frequency can fit the damping coefficient after the determination of the effective Young's modulus. Fig. 2-17 shows the responses with different convective heat transfer coefficients, and convective coefficients only affect the response in the low frequency region. By measuring the frequency response of deflection, the effective Young's modulus, the damping coefficient, and the convective heat transfer coefficients can be known in order. Similarly, Fig. 2-18 to Fig. 2-20 show the similar deflection frequency responses of the bilayer cantilever with the tip heating case. The fitting of these three parameters of tip input model are shown in Fig. 2-18, Fig. 2-19, and Fig. 2-20 respectively. The fitting of experimental results are demonstrated in Chapter 3.3.

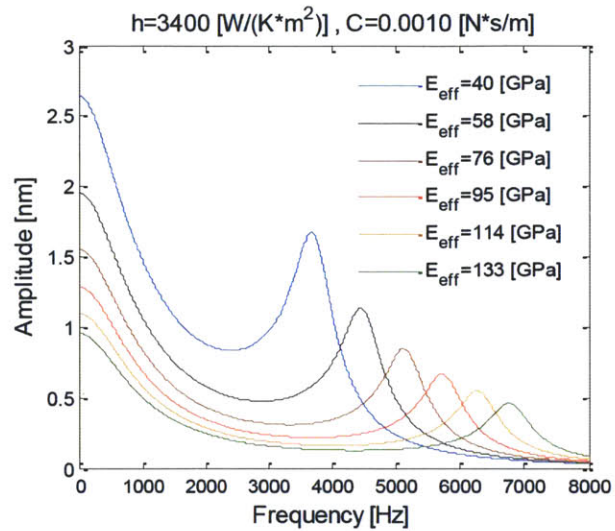


Figure 2-15 : Deflection frequency responses of the bilayer cantilever with uniform heating calculated with different effective Young's modulus. The effective Young's modulus is used to fit the resonant frequency.

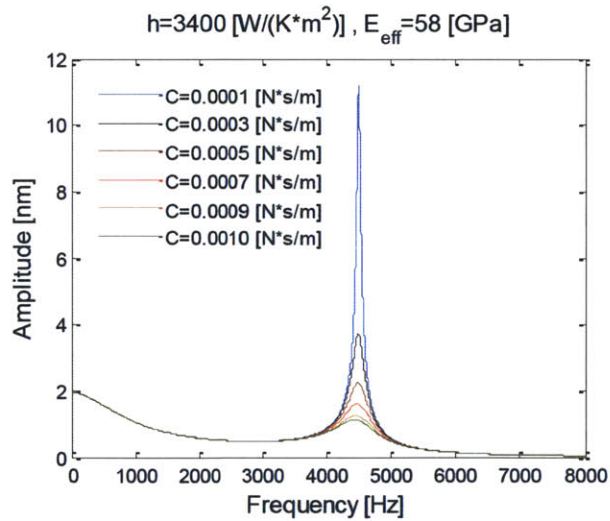


Figure 2-16 : Deflection frequency responses of the bilayer cantilever with uniform heating calculated with different damping coefficients. The damping coefficient is used to fit the peak and width of the resonant frequency.

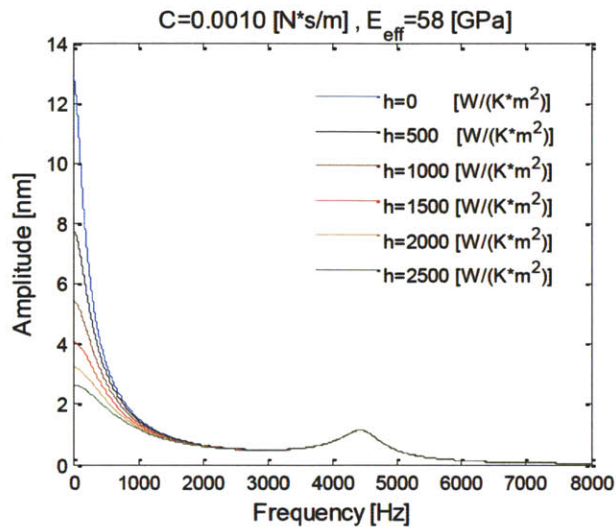


Figure 2-17 : Deflection frequency responses of the bilayer cantilever with uniform heating calculated with convective heat transfer coefficients. The convective heat transfer coefficient is used to fit the curve in the low frequency region.

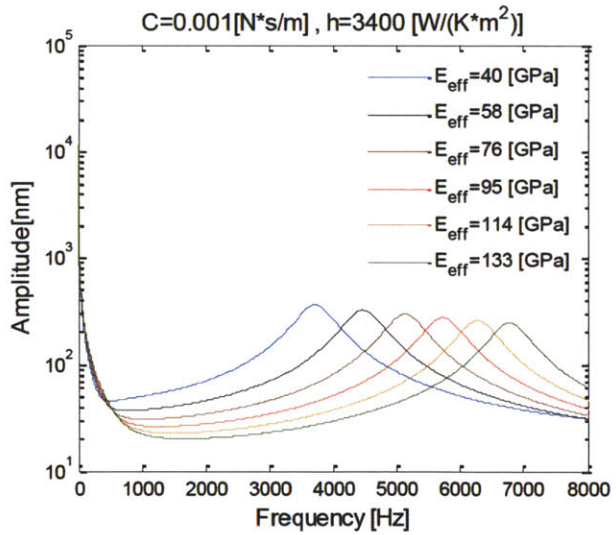


Figure 2-18 : Deflection frequency responses of the bilayer cantilever with tip heating calculated with different effective Young's modulus. The effective Young's modulus is used to fit the resonant frequency.

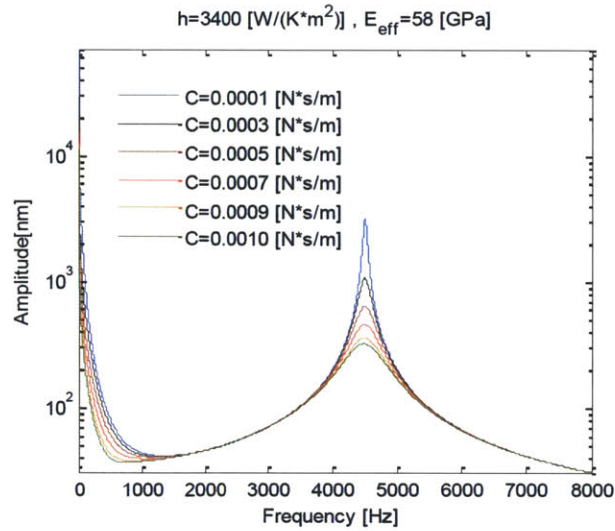


Figure 2-19 : Deflection frequency responses of the bilayer cantilever with tip heating calculated with different damping coefficients. The damping coefficient is used to fit the peak and width of the resonant frequency.

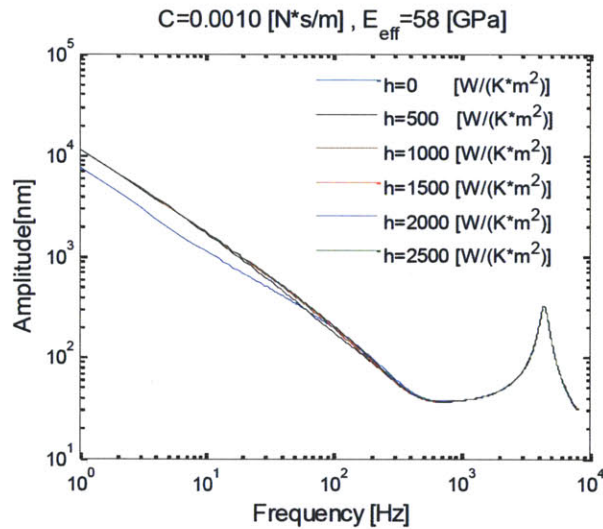


Figure 2-20 : Deflection frequency responses of the bilayer cantilever with tip heating calculated with convective heat transfer coefficients.

Chapter 3

Calibrations for Quantitative Measurements

For quantitative spectra measurements, the system requires four calibrations: the background spectrum calibration, beam intensity distribution calibration, frequency response calibration and power calibration. Section 3.1 shows the background spectrum calibration. Section 3.2 considers the non-homogeneous beam intensity from the optical fiber. Section 3.3 compensates the signal reduction due to the frequency response of the bilayer cantilever. Section 3.4 calibrates the deflection of the cantilever to the absolute absorbed power. Section 3.5 summarizes the calibrations as a total calibration factor.

3.1 Background Spectrum Calibration

First, the background spectrum calibration is needed to calibrate variations in the spectral intensity of the light source as well as atmospheric absorption. The absorbance spectrum can then be calculated by dividing the absorbed power spectrum with the incident power spectrum.

The incident power spectrum, shown in Fig. 3-1, is measured by a FTIR system

(PerkinElmer Spectrum GX) after the beam passes through the polycrystalline infra-red (PIR) fiber. Fig. 3-1(a) shows the spectrum in wavelengths, and Fig. 3-1(b) changes the x axis from wavelength to modulated frequency using equation (7). Note that the y axis is in unit of arbitrary, so the background spectrum calibration is needed to convert the arbitrary unit to the absolute power.

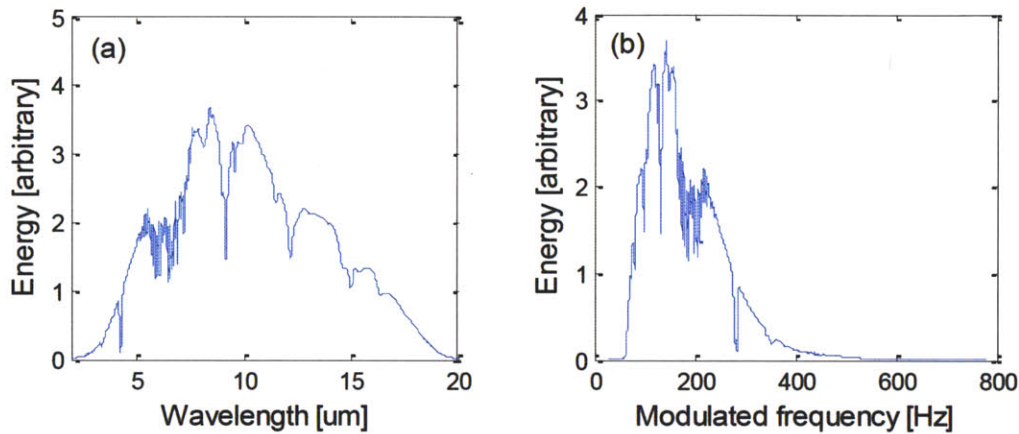


Figure 3-1 : Incident power spectrum exiting from the polycrystalline infra-red fiber. This spectrum is measured by a FTIR system (PerkinElmer Spectrum GX). (a) The spectrum plots with wavelengths. (b) The spectrum plots with modulated frequencies that is transformed by equation (7).

In this thesis, the exit power of the infrared beam passing through the PIR fiber is called the fiber power. Fiber power can be calibrated by assuming the proportionality between the power and the total spectral area. Fig. 3-2 shows the spectra of different sizes of B-stop without the passing through the PIR fiber. B-stop is an iris that is used to control the size of the incident beam. Thermopile (Newport, High Sensitivity Thermopile Sensor, Model : 818P-001-12) measures the incident power with each size of B-stop, and the values are in Table 3. Each column stands for the estimation of one B-stop value. The first row indicates the B-stop value. The second row is the background power that is averaged by 90000 samples from the thermopile, and the

third and fourth rows show their standard deviation and relative errors respectively. The background spectral areas, $A_{background}$, measured by FTIR are listed in the fifth row, so the estimated power from PIR fiber in the sixth row are calculated by

$$P_{fiber} = P_{background} \cdot \frac{A_{fiber}}{A_{background}} \quad (52)$$

$P_{background}$ is the total background power of each B-stop size, A_{fiber} is the spectral area of fiber. Finally, the averaged estimated total power from the PIR fiber is $197.3\mu\text{W}$.

Table 3. The fiber power estimated by the FTIR and thermopile.

B-stop[cm]	1.3	2	4	6	8	10	12	14	16	18	20
BG power [mW]	0.809	1.025	2.328	4017	7.243	10.35	13.61	17.16	21.00	23.00	26.04
std. dev. [uW]	28.02	41.20	30.60	131.6	18.05	37.35	76.52	133.1	118.3	91.86	55.34
Power error [%]	3.46	4.02	1.31	3.16	0.249	0.361	0.562	0.776	0.563	0.383	0.216
BG Area [arb.*cm ⁻¹]	4031	7380	23459	48976	81470	120322	158846	198147	223418	243919	253369
Estimated fiber power [mW]	0.456	0.313	0.224	0.192	0.2001	0.194	0.193	0.195	0.209	0.222	0.232
fiber area [arb.*cm-1]	2254.97										
Averaged fiber power [mW]	0.1973±0.0065										

Note 1: Measurement of thermopile sets its reference at 1064nm, 90000 samples at sample rate 0.1ms, mirror velocity at 0.12 cm/s, J-stop at 6.48 cm^{-1} , resolution at 8 cm^{-1} .

Note 2 : BG stands for background.

Note 3 : Averaged fiber power considers the fiber power with B-stop of 8, 10, 12, 14, 16 and 18cm, because the relative error is smaller than 1%. Since the beam size of 20cm B-stop is larger than the size of thermopile, it should not be considered as well.

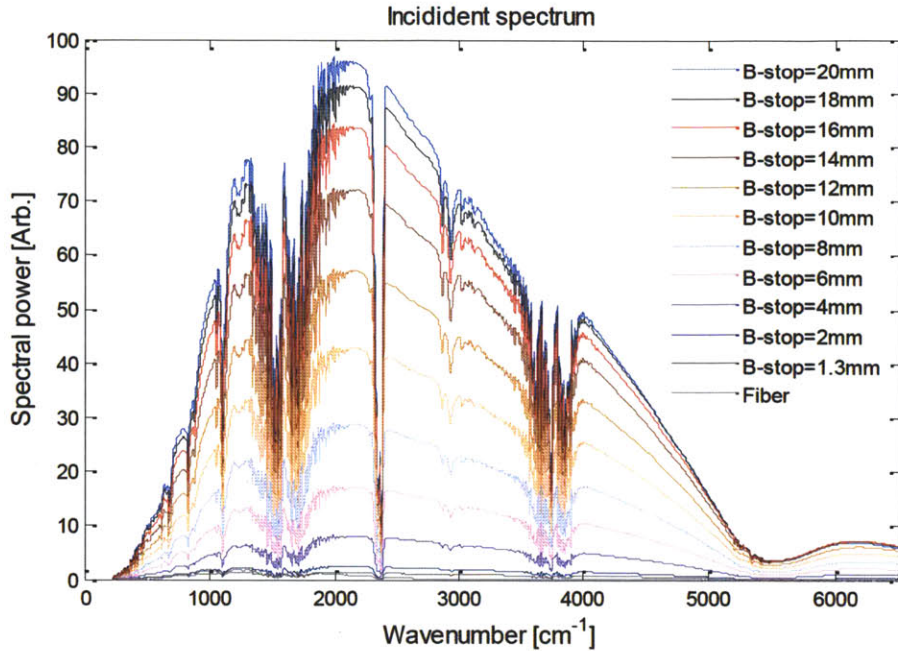


Figure 3-2 : Background spectra measured by a Fourier transform infrared system with different B-stop values. The spectra are also measured by a FTIR system (PerkinElmer Spectrum GX). The assumption of the proportionality between the absolute power and the area under each curve are made to estimate the power from the PIR fiber.

3.2 Beam Intensity Distribution Calibration

Second, the beam intensity distribution calibration takes into account the non-uniform intensity output profile from the PIR fiber. Since the incident input power varies with position, the intensity distribution and the alignment of the sample to the PIR fiber must be known with a high degree of precision. Illustrating this point is a schematic of a typical beam spot incident on a portion of a cantilever, shown in Fig. 3-3. The beam intensity profile has been measured by the IR camera in Fig. 2-8 and Fig. 2-9, and use the Gaussian function fitted in Fig. 2-9 to calculate the two-dimensional (2D) intensity distribution of Fig. 3-4. This 2D intensity distribution has already considered the divergence with the distance of $\sim 200 \mu\text{m}$ with the

numerical aperture (NA) of 0.25 (The value of NA=0.25 is provided from JT Ingram Technology Inc.). Based on the picture of Fig. 3-3(b), the intensity portion covered by the cantilever can be determined, and it is shown in Fig. 3-5. The incident intensity on cantilever after beam intensity distribution calibration is 3.3 μW , and it is used to normalize the total area of Fig. 3-1(b). Note that it is incorrect to normalize the total area of Fig. 3-1(a) to 3.3 μW . The reason is that the FTIR plots its spectral power in terms of wavenumber ($E_{b\eta}$) instead of wavelength ($E_{b\lambda}$), and the modulated frequency is proportional to the wavenumber. To integrate the consistent total power, it requires

$$\int E_{b\lambda} d\lambda = \int E_{b\eta} d\eta \quad (53)$$

where

$$E_{b\lambda}(T, \lambda) = \frac{2\pi h_p c_0^2}{h_p c_0} \frac{1}{n^2 \lambda^5 [e^{\frac{h_p c_0}{n \lambda k_b T}} - 1]} \quad \text{and} \quad E_{b\eta}(T, \eta) = \frac{2\pi h_p c_0^2 \eta^3}{h_p c_0 \eta} \frac{1}{n^2 [e^{\frac{h_p c_0 \eta}{n k_b T}} - 1]} \quad (54)$$

h_p is the Planck's constant, c_0 is the speed of light, k_b is the Boltzmann's constant, n is the refractive index of medium, T is the temperature, λ is the wavelength of light, and η is the wavenumber of light. Finally, the incident input power spectrum is calibrated and shown in Fig. 3-6.

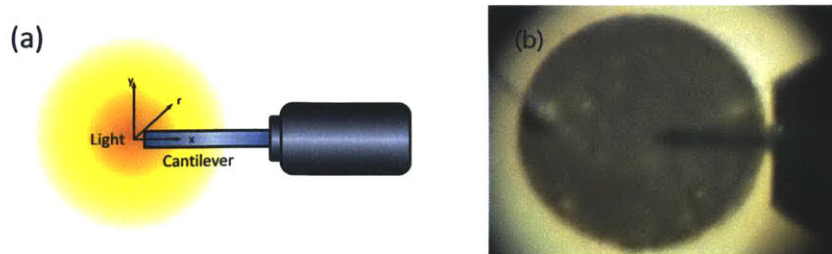


Figure 3-3 : Schematic of the beam intensity distribution calibration. The beam spot from the PIR fiber is typically larger than the cantilever. As a result, the incident input power will depend on the position of the cantilever within the beam spot due to a non-uniform beam intensity profile. (a) The schematic of the coordinate. (b) The actual position of the cantilever with respect to the PIR fiber.

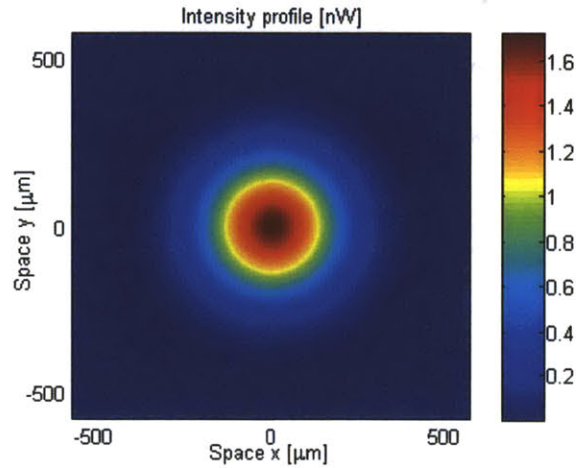


Figure 3-4 : Two dimensional intensity profile. The fitting intensity profile uses the Gaussian function in Fig. 2-9. This profile distribution has already considered the divergence with the distance of $\sim 200 \mu\text{m}$ and the numerical aperture (NA) of 0.25 (The value of NA=0.25 is provided from JT Ingram Technology Inc.).

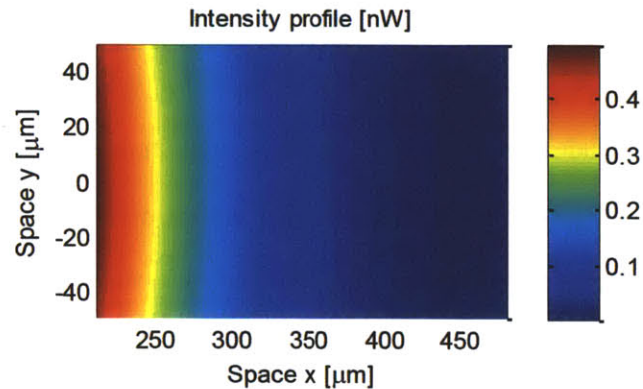


Figure 3-5 : Two dimensional incident intensity on the cantilever. The incident intensity on the cantilever is cut out a portion from Fig. 3-4 based on the Fig. 3-3(b), and the incident intensity after beam intensity distribution calibration is $3.3 \mu\text{W}$.

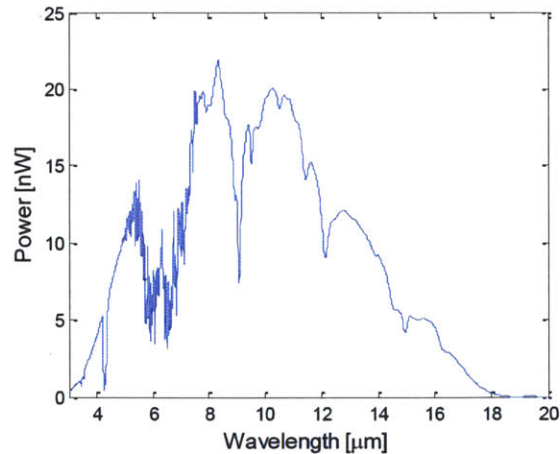


Figure 3-6 : Incident input power spectrum after background and beam intensity distribution calibrations. This spectrum shows the absolute spectral power exiting from the PIR fiber. The total incident power is $3.3 \mu\text{W}$.

3.3 Frequency Response Calibration

Third, the frequency response calibration accounts for the phase delay of the periodic heat input conducting through the cantilever at the different light modulation frequencies. This phase delay, which is dependent on the thermal diffusivity of the cantilever, will lead to a reduction of the deflection amplitude at higher modulation frequencies. To characterize the frequency response of the cantilever, an additional modulated laser (Model: LTC6704A5-T from Lasermate Group, Inc.) is used to heat up periodically with a 50% duty cycle. Fig. 3-7 shows the frequency response data measured for a Si/Al cantilever in air. Each data point represents the vibration amplitude measured by the PSD at the chosen modulating frequency. A peak resonance can be observed around 4550 Hz, and this corresponds to the resonance frequency of the cantilever, and it is a confirmation of the cantilever-type probe. Theoretical curve of the uniform heating model is used to fit the experimental data with $C=0.0007[\text{N}\cdot\text{s}/\text{m}]$, $h=500[\text{W}/(\text{K}\cdot\text{m}^2)]$, and $E_{\text{effective}}=60 [\text{GPa}]$. The convective

heat transfer coefficient agrees with the estimation of the empirical equation from natural convection.³³

More importantly, the frequency response of deflection can be observed that the amplitude decreases with increasing frequency. Therefore, to maintain a measurable signal while avoiding low frequency noise, the working region is chosen to be in the range of 30-1000 Hz, illustrated in Fig. 3-8. Using these data, the cantilever deflection amplitude reduction induced by the periodic heat input over the entire range of modulated incident light frequencies from the interferometer can be accounted for.

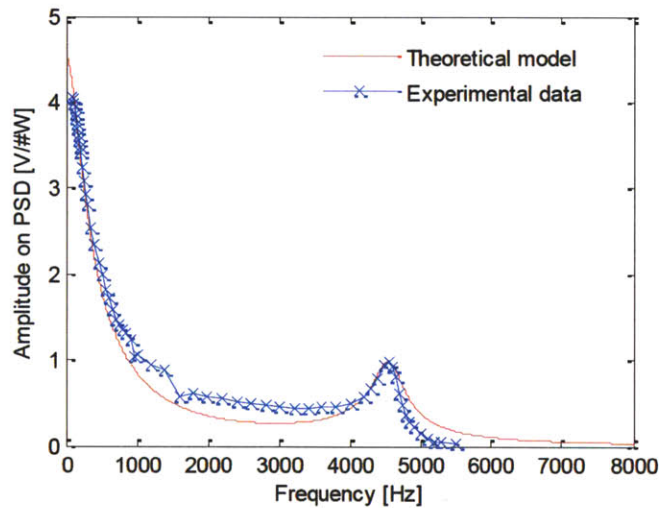


Figure 3-7 : Experimental and theoretical frequency response of the Si/Al cantilever. The experimental frequency response of the Si/Al cantilever shows the resonant frequency about 4550Hz. The theoretical curve of the uniform heating model is used to fit the data with $C=0.0007[N*s/m]$, $h=500[W/(K*m^2)]$, and $E_{effective}=60 [GPa]$. Each data point represents the deflection amplitude on the PSD where the intensity of the input is constant.

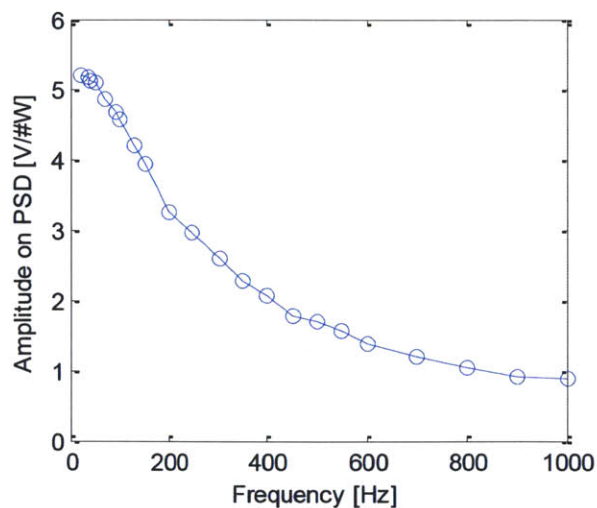


Figure 3-8 : Operating range of frequency response of the bilayer Si/Al cantilever. Frequency response of a rectangular Si/Al cantilever covers the working range of the FTIR. Each data point represents the deflection amplitude on the PSD where the intensity of the input is constant.

3.4 Power Calibration

Finally, the power calibration correlates the oscillating amplitude measured by the PSD to the absolute power absorbed by the cantilever. Three steps are required. First, the incident power on the cantilever is obtained by subtracting the bypassed power from the incoming power. The bypassed power ($0.1089 \pm 0.001\text{mW}$) and incoming power ($2.893 \pm 0.05\text{mW}$) are measured using a photodiode (Model: 818-UV) from Newport (Fig. 3-9 and Fig. 3-10). Second, the absorptance of the metal film, aluminum in this case, is measured using a conventional spectrometer by depositing metal on a Si wafer using the same Physical Vapor Deposition (PVD) process as for the cantilever. The metal is optically thick so that substrate effects are negligible. The absorptance of the 250nm aluminum film is 0.11877. After measuring the absorptance, the absorbed power ($0.3307 \pm 0.017\text{mW}$) on the cantilever can be calculated by multiplying the absorptance with the incident power of $2.784 \pm$

0.05mW. Note that the absorbed power is obtained in this manner because the scattered power is difficult to determine. Third, an arbitrary modulation frequency is chosen as reference for the absolute power absorbed in the frequency response of Fig. 3-8. The deflection amplitude on the PSD then correlates to the known absorbed power on the cantilever at the given frequency. Subsequently, correction factors for absorbed power versus deflection amplitudes at other frequencies can be determined in unit of voltage per watt using the frequency response data of Fig. 3-8, and hence, the calibrated frequency response of the Si/Al cantilever is shown in Fig. 3-11.

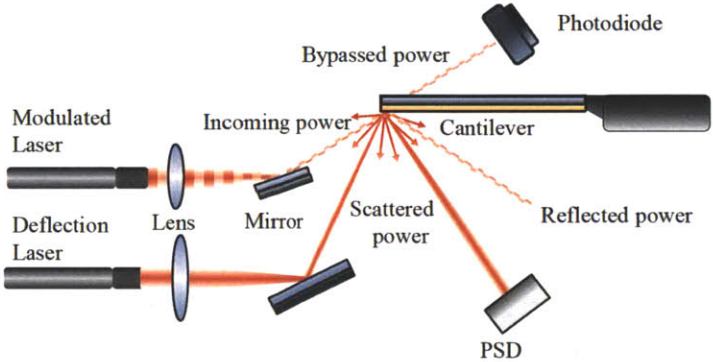


Figure 3-9 : System configuration used in the power calibration. A separate laser from the deflection measurement laser is modulated to associate the frequency response with a calibrated power input. The incoming power ($2.983 \pm 0.05\text{mW}$) and bypassed power ($0.1089 \pm 0.001\text{mW}$) are measured using a photodiode. The incident power ($2.784 \pm 0.05\text{mW}$) is calculated by subtracting the bypassed power from the incoming power. The absorptance of the aluminum coating is 0.11877 measured in a spectrometer. Hence, the absorbed power ($0.3307 \pm 0.017\text{mW}$) is the product of the absorptance and the incident power.

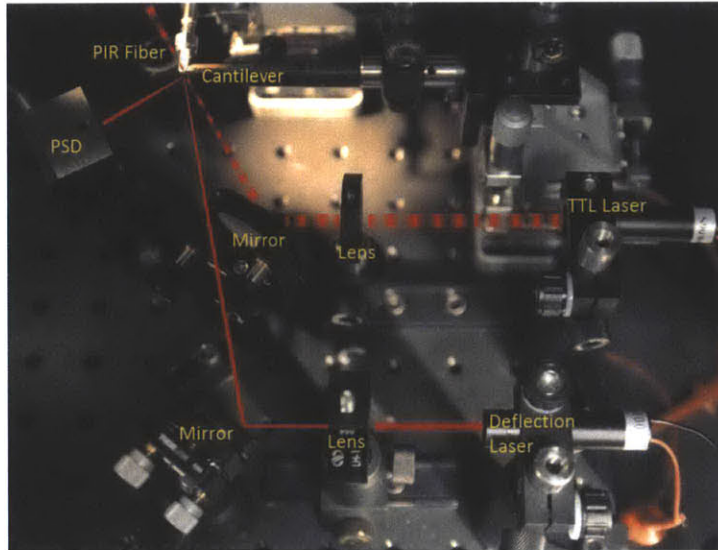


Figure 3-10 : Experimental setups for the power calibration. Experimental setups are carried out on an optical breadboard consisting of one deflection laser, one transistor-transistor-logic (TTL) modulated laser, two focused lenses, two mirrors, one PSD, one PIR fiber, and the Si/Al bilayer cantilever.

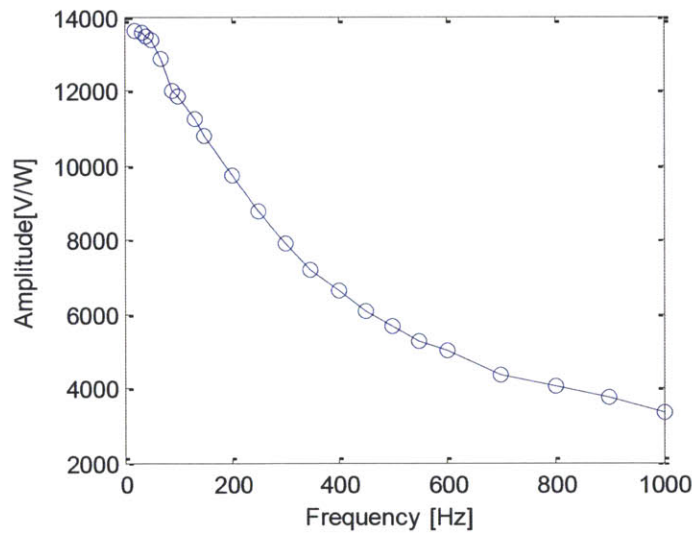


Figure 3-11 : Frequency response of the Si/Al cantilever after the power calibration. This frequency response is shown from 0 to 1000Hz, which is the operating range. The y axis now stands for the amplitude on PSD with 1W absorbed power by using the setup in Fig. 3-10.

3.5 Total Calibration Factor

To sum up, the calibrations can be described as a product of four factors as follow:

$$f_T(\vec{r}, \omega) = f_B(\omega) \cdot f_I(\vec{r}) \cdot f_F(\omega) \cdot f_P$$

where $f_T(\vec{r}, \omega)$ is the total calibration factor. $f_B(\omega)$ is the background spectrum calibration factor that measures the incident power spectrum exiting from the PIR fiber. $f_I(\vec{r})$ is the beam intensity distribution calibration factor, which considers the incident intensity covered by the sample. The frequency calibration factor, $f_F(\omega)$, compensates the reduction of amplitude due to the phase delay of thermal diffusion. The power calibration factor, f_P , calibrates the amplitude signal on PSD to the absolute absorbed power. \vec{r} is the spatial position, and ω is the modulation frequency. $f_B(\omega)$ and $f_F(\omega)$ are frequency dependent, and $f_I(\vec{r})$ is space dependent. Once these four calibrations are measured, quantitative measurements can be carried out by multiplying these factors with the raw data.

Chapter 4

Experimental Validation

To validate the proposed system, the absorptance of a silicon/aluminum cantilever was measured. Section 4.1 shows the absorptance of a silicon/aluminum thin film from calculations of the transfer matrix method. Section 4.2 offers the raw data measured by the bilayer cantilever. Section 4.3 provides the absorbed power spectra from calibrations. The absorptance spectra are shown in the Section 4.4.

4.1 Absorptance of the Si/Al thin film

The transfer matrix method offers the estimation of the absorptance of a silicon/aluminum thin film.^{41,42} Fig. 4-1 and Fig. 4-2 calculates the absorptance incident on the silicon side from the transfer matrix method using the Table 1 and optical constants of different dopant concentrations of the n-typed silicon layer.⁴³ The resistance of the silicon layer is 0.01-0.025 [$\Omega \cdot \text{cm}$], which is provided by the NanoWorld, and its corresponding concentration is $1 \times 10^{18} \sim 5 \times 10^{18} [\text{cm}^{-3}]$.⁴⁴ Two peak wavelengths do not vary significantly in the concentration range of 10^{17} - $10^{19} [\text{cm}^{-3}]$ (Fig. 4-1), and they change with the thickness of the silicon layer

(Fig. 4-2). These two properties are available to fit the experimental data independently. The fitting result is shown in Section 4.4.

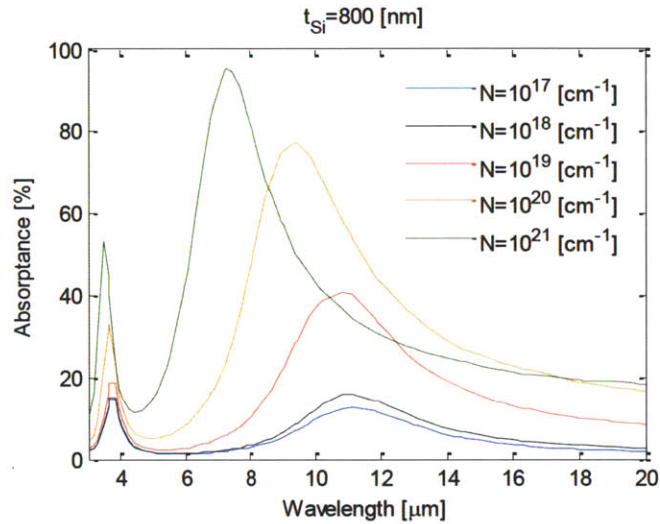


Figure 4-1 : Absorbance of the silicon/aluminum thin film with different doping concentration. The absorbances are incident on the silicon side and calculated based on the transfer matrix method with different n-type dopant concentrations. The two peak wavelengths are nearly constant in the concentration range of 10^{17} - 10^{19} [cm^{-3}]

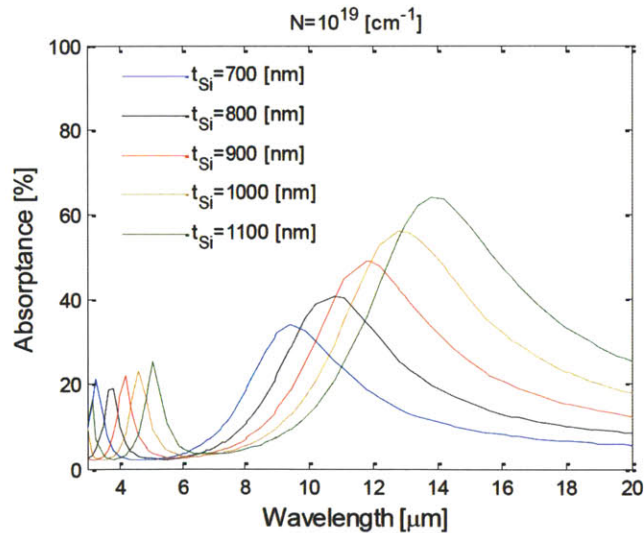


Figure 4-2 : Absorbance of the silicon/aluminum thin film with different thickness of the silicon layer. The absorbances are a function of the thickness of the silicon layer for light incident from the silicon side.

4.2 Raw Data

The periodic light input from the interferometer on the cantilever changes the absorbed power in the sample with respect to time, and consequently the temperature of the cantilever varies in time. Hence, the bilayer cantilever will deflect in an oscillating pattern, and the laser beam reflected on the metallic side of the cantilever to a PSD is used to measure the deflection pattern of the cantilever.

A silicon/aluminum cantilever is chosen for demonstration purposes. Fig. 4-3 shows the deflection signal from a Si/Al cantilever during a typical measurement. The modulated light is incident on the silicon layer, and Fig. 4-3 displays the oscillating deflection signal captured by the PSD with different velocities of mirror. Since the modulated light intensity combines components of many frequencies, an interferogram-patterned signal can be observed in the time domain. The faster velocity modulates the intensity to the higher frequency, so the interferogram in the time domain with the higher velocity constrains in a shorter period. Taking the fast Fourier transform of the signal in Fig. 4-3 generates the spectral component of the signal, more precisely the spectrum of absorbed power (Fig. 4-4). These absorbed spectra in Fig. 4-4 are averaged by 50 scans and using the data acquisition 6210 from National Instruments (NI) with the sampling rate of 250,000 samples per second acquired over 1 second. Fig. 4-5 shows the averaged background spectrum, and vibrational noises around 30Hz and 230Hz and electric noises at 60Hz, 120Hz, 180Hz, and 240Hz are the dominant errors. Fig. 4-6 subtracts the background spectrum from the absorbed spectra in Fig. 4-4. The reductions of level of the absorbed spectra are due to the frequency response of deflection, and they are compensated by the

frequency response calibration in Section 4.3. Note that the corresponding signals at the frequencies of electric noises have significant errors due to the nature of non-random vibrations. Avoiding from the electric noise, the velocity of mirror can be adjusted.

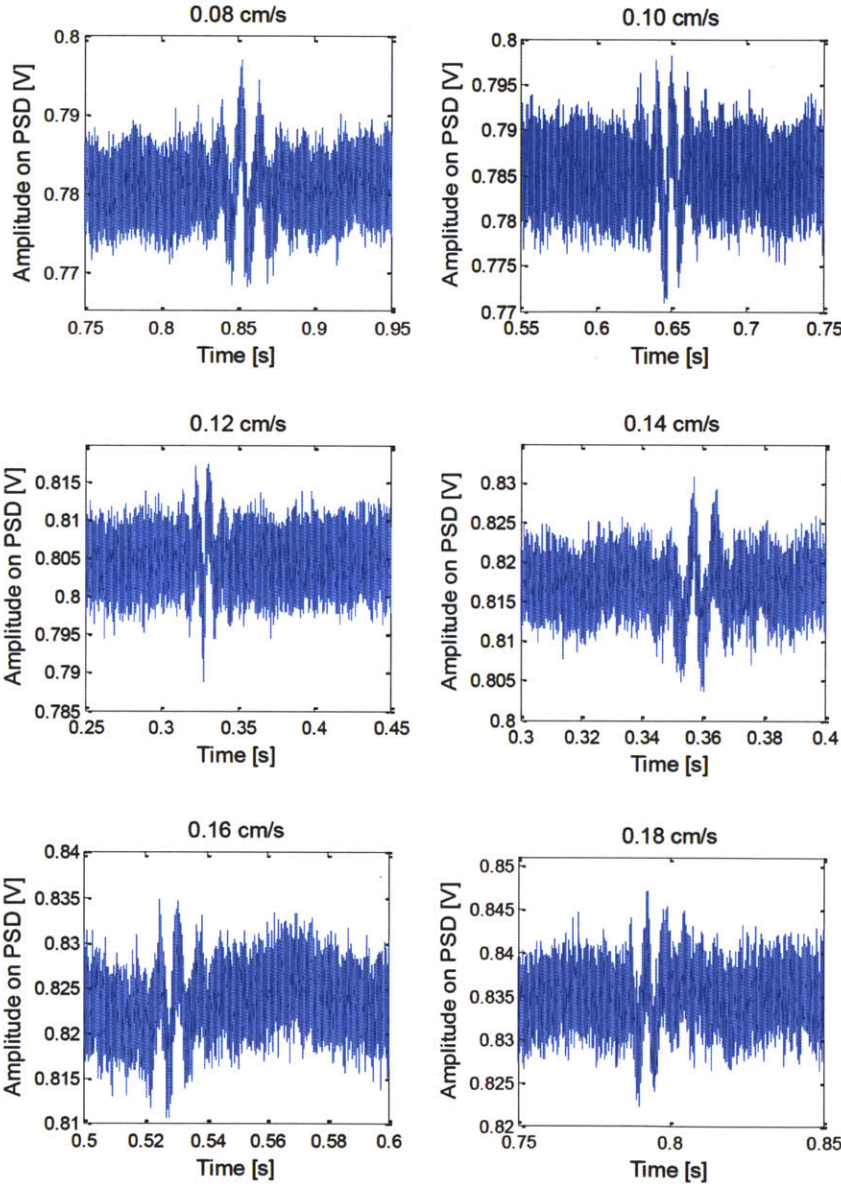


Figure 4-3 : Deflection signals of the Si/Al cantilever in time domain captured by the position sensitive detector with different velocities of mirror. Since the modulated light intensity combines components of many frequencies, an interferogram-patterned signal is observed. The faster velocity modulates the intensity to the higher frequency, so the interferogram in the time domain constrains in a shorter period.

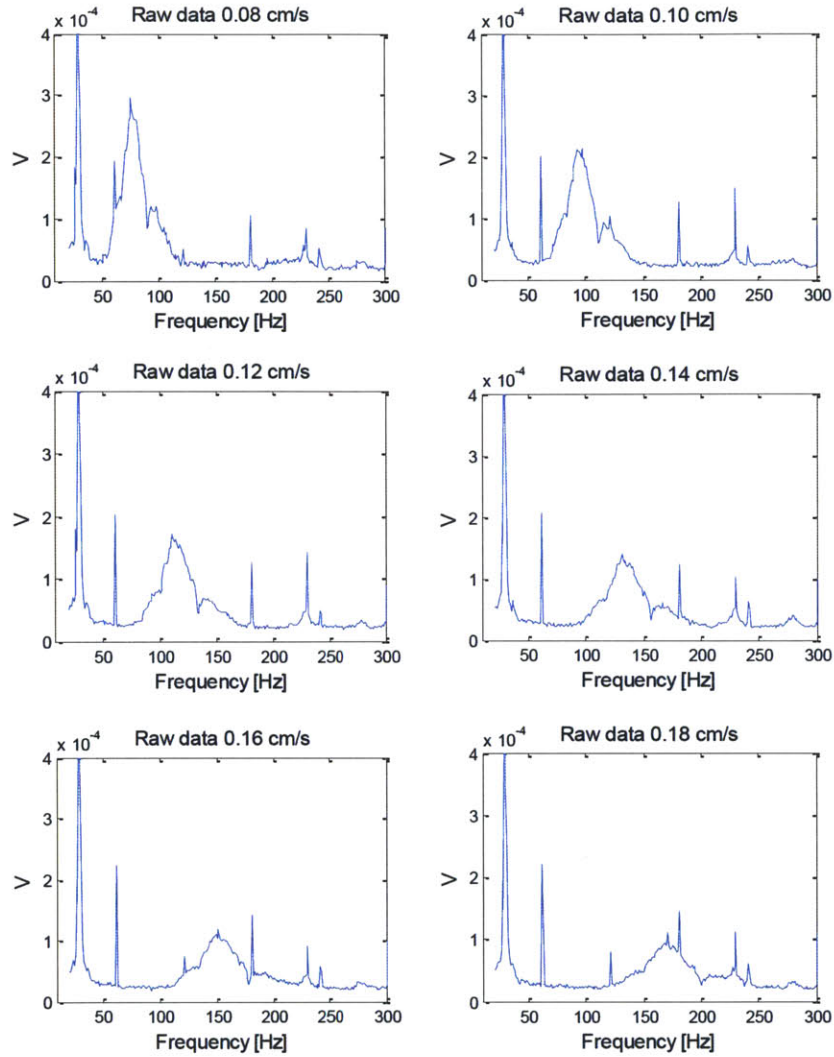


Figure 4-4 : Absorption spectra of the Si/Al cantilever with different velocities of mirror. Each spectrum is averaged over 50 scans. Before subtracting the background spectrum, the electric and vibrational noises are clearly seen.

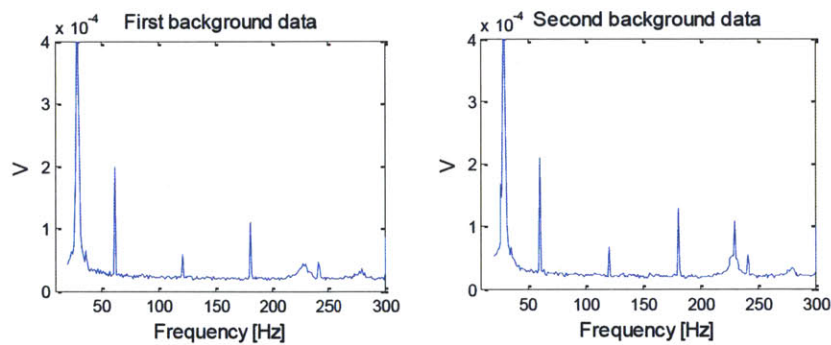


Figure 4-5 : Background spectra of the Si/Al cantilever. The first background data are recorded before measurements, and the second background data are recorded after measurements.

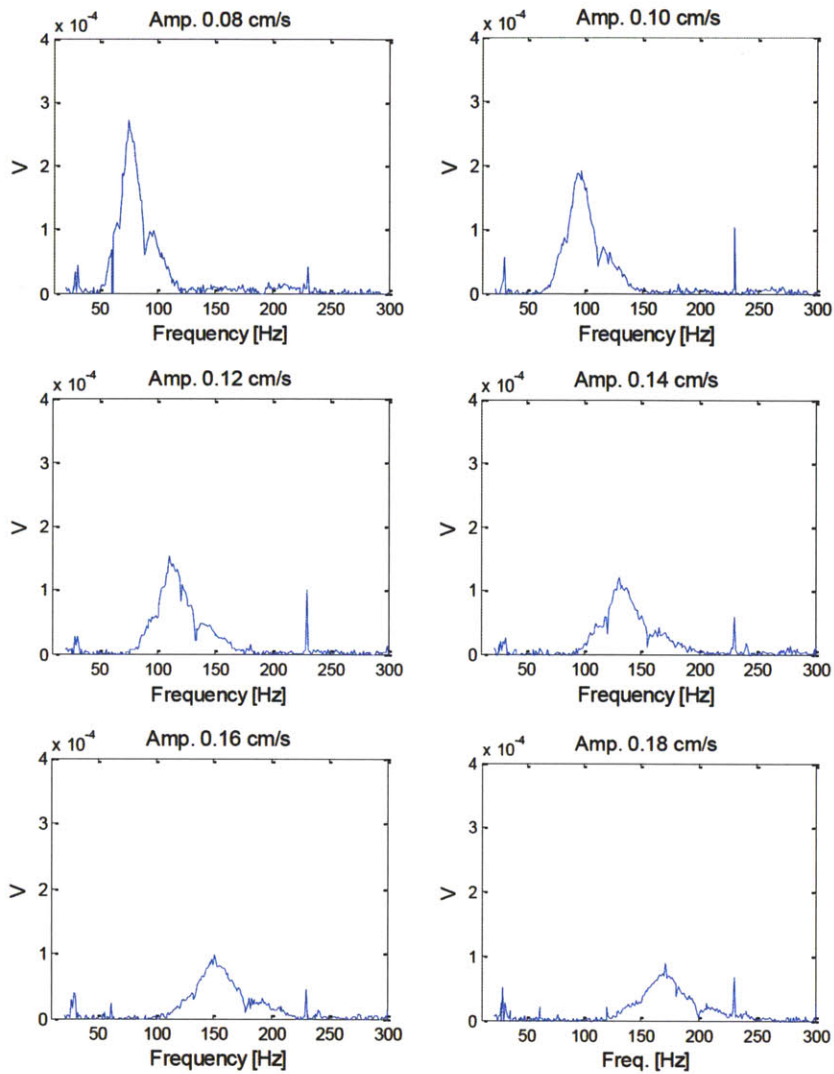


Figure 4-6 : Absorption spectra of the Si/Al cantilever after subtracting the background spectrum. The spectra of different velocities of mirror are shown in different frequency region. The reductions of level of the absorbed spectra are due to the frequency response of deflection, and they are compensated by the frequency response calibration.

4.3 Data Calibrations

To quantitatively derive the absorbance spectra, four calibrations in Chapter 4 are needed to compensate for the data. The absorbance spectra are the ratio of the absolute absorbed power spectra to the incident power spectrum. The incident power

spectrum is known in Section 3.1 and 3.2. Absolute absorbed power spectra are calculated by dividing the absorbed spectra of Fig. 4-6 by the frequency response curve of Fig. 3-11, and the calibrated spectra are shown in Fig. 4-7. The frequency response curve has considered the frequency response and power calibration. Finally, following the principles of the Michelson interferometer, frequencies of Fig. 4-7 can be converted to their corresponding wavelengths and divided by the incident power spectrum of Fig. 3-6, and the absorbance spectra are provided in Fig. 4-8. FTIR provides constant wavenumber resolution during the scanning, so different velocities offers different wavelength resolutions. Each blue point of the absorbance spectra represents each measured data point.

The small discrepancy of the absolute absorbed power spectra of Fig. 4-7 is due to the frequency response calibration. There are two possible reasons. First, the larger driving amplitude (1~5.5V in Fig. 3-8) of the frequency response can change the convection heat transfer coefficient; however, the amplitude (< 30 mV) of the FTIR measurement is much smaller, so the inconsistent convection coefficient may change the curve of frequency response. Second, FTIR uses the modulating intensity with the sinusoidal shape that is different from the rectangular shape in the frequency response calibration, because the TTL modulated laser provides square pulse intensity only.

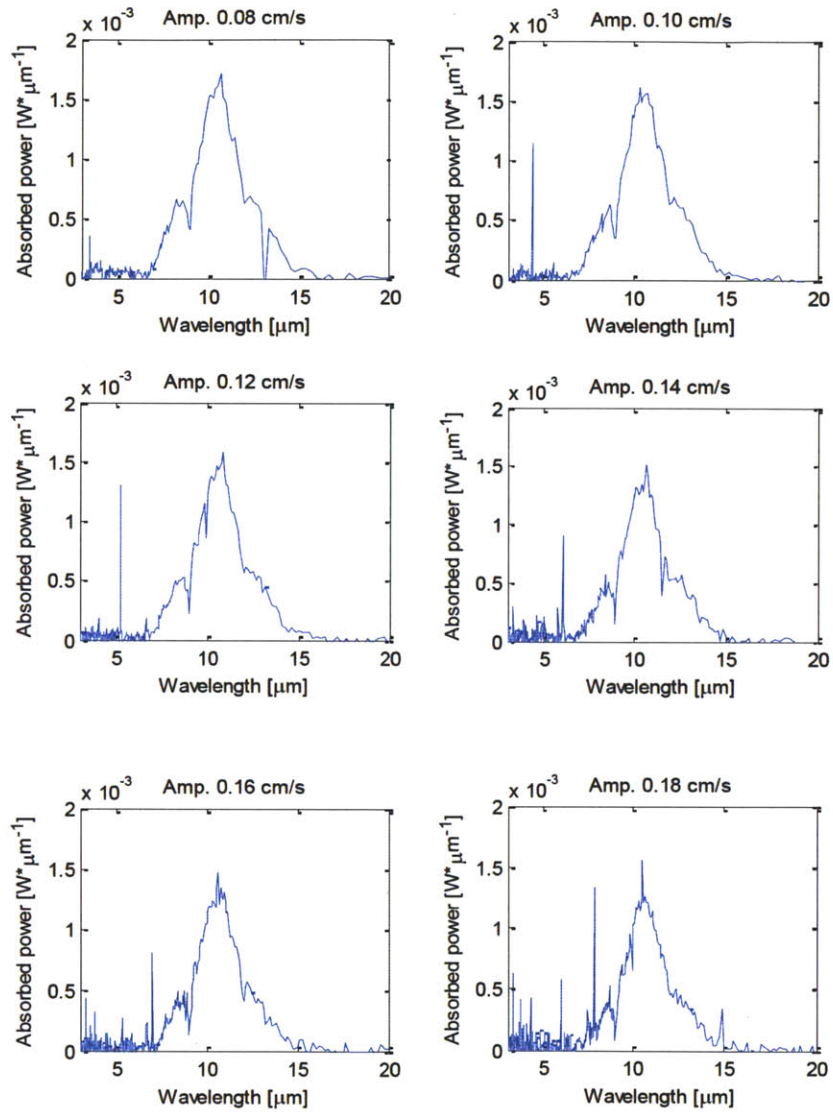


Figure 4-7 : Absolute absorbed power spectra of the Si/Al cantilever after the frequency response calibration. The discrepancy between absolute absorbed power spectra of different velocities of mirror may be due to the frequency response calibration.

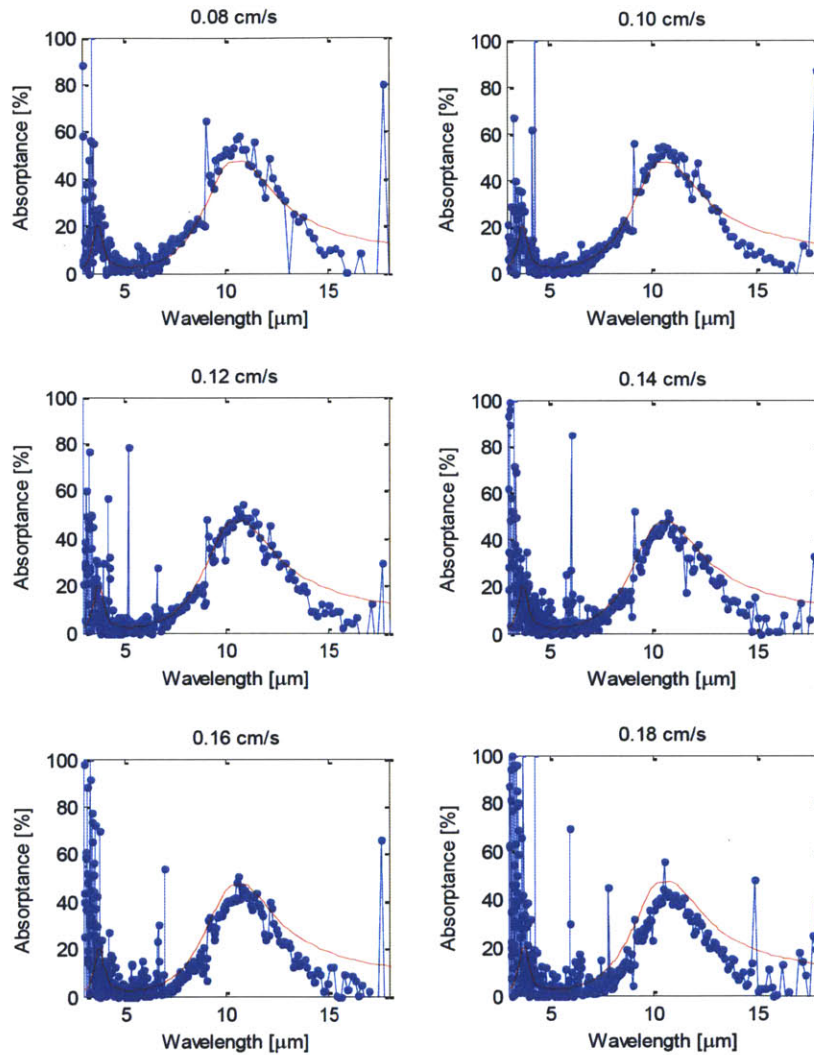


Figure 4-8 : Absorbance spectra with the theoretical calculation and experimental measurements of different velocities. Theoretical curve is calculated with the dopant concentration of $1.1 \times 10^{19} \text{ [cm}^{-3}\text{]}$ and the dimension in Table 1. FTIR provides constant wavenumber resolution during the scanning, so different velocities offers different wavelength resolutions. Each blue point of the absorbance spectra represents each measured point.

4.4 Summary and Results

To summarize the measurements, Fig. 4-9 shows the flow diagram of calibrations. Background spectrum and beam intensity distribution calibrations provide the incident power spectrum, and the frequency response and power calibrations compensate the absorbed power spectra. The averaged absorbance spectrum can be extracted by dividing the absorbed power spectra by the incident power spectrum.

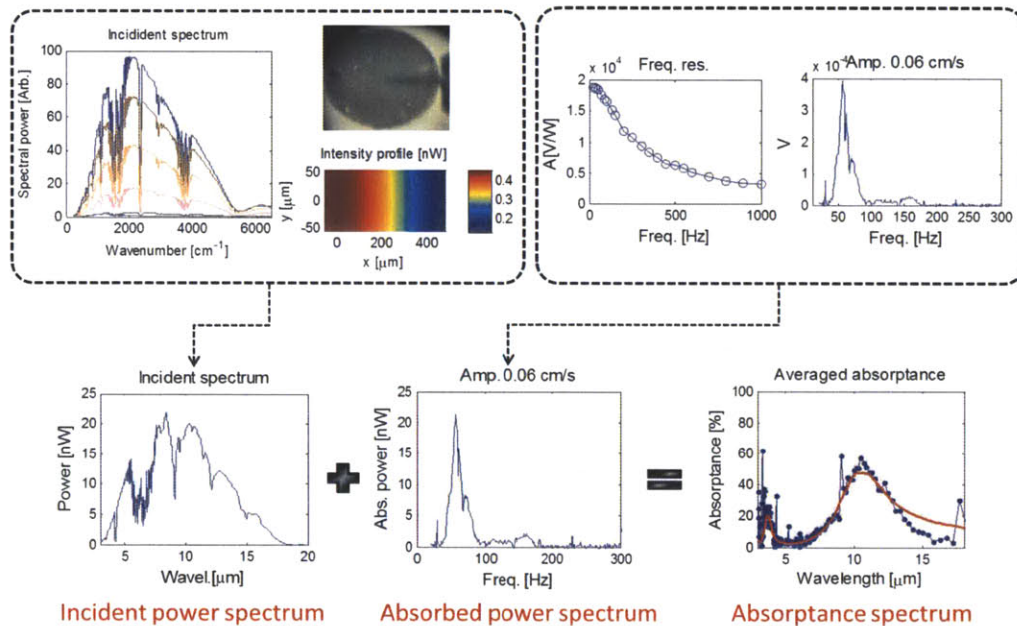


Figure 4-9 : Flow diagram of the calibrations. Background spectrum and beam intensity distribution calibrations provide the incident power spectrum, and the frequency response and power calibrations compensate the absorbed power spectrum. The averaged absorbance spectrum can be extracted.

For the Si/Al cantilever, the theory matches well with the quantitative averaged results of experiment, as shown in Fig. 4-10. The theoretical results were calculated using the transfer matrix method with the geometric dimensions previously

specified in Table 1, and the n-type silicon with a dopant concentration of $1.1 \times 10^{19} \text{ [cm}^{-3}\text{]}$. The variation of thickness variation of the silicon layer provided by Nanoworld ranges from 500 nm to 2500 nm, and 800 nm is used to fit the experimental results.

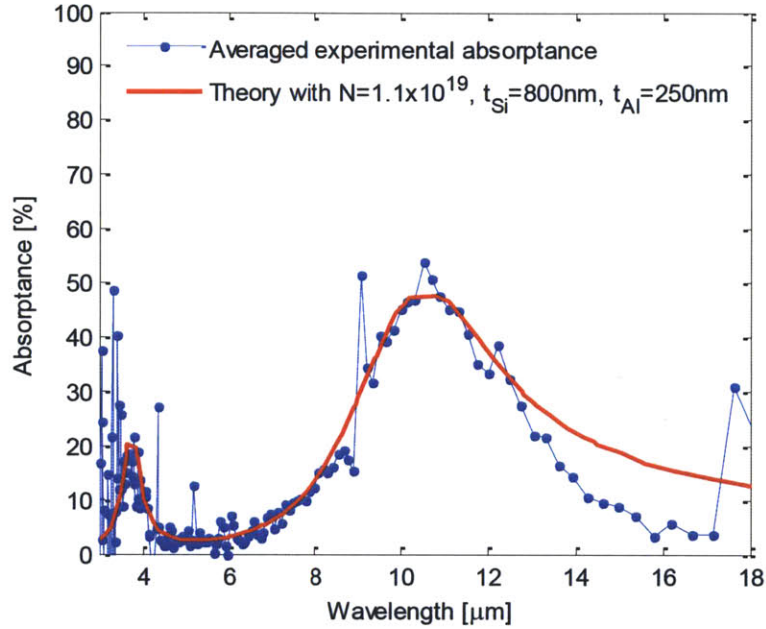


Figure 4-10 : Averaged absorbance of experimental measurements with the theoretical calculation. This absorbance spectrum is averaged by six curves of different velocities in Fig. 4-8, and it uses data points of 0.06[cm/s] as the reference. Theoretical curve is calculated with the dopant concentration of $1.1 \times 10^{19} \text{ [cm}^{-3}\text{]}$ and the dimension in Table 1.

Table 4 provides the error of each measurement, and the valued ranges are calculated due to the accumulating errors. Background spectrum calibration estimates the PIR fiber output power using the spectral area offered by the FTIR system, and its relative error is 0.815%. Given a value of the PIR fiber, the relative error of the beam intensity distribution calibration is 121.2%; however, considering the error of background spectrum calibration, the incident power can shift from $1.5\mu\text{W}$ to $7.4\mu\text{W}$. To quantify the error of the frequency response calibration, the absolute absorbed

power spectra of Fig. 4-7 are considered, and the peak absorbed power of 11 μ m are chosen as the indication. For the absorbed power, the relative errors of the frequency response calibration and the power calibration are 12.33% and 5.14% respectively. Finally, the absorptance has the relative error of 4.85% considering the incident power of $3.3 \pm 4\mu$ W, and it can shift from 21.29% to 105.0% at the wavelength of 11 μ m considering the incident power of the accumulating errors.

Table 4. The error of each measurement.

	Calibration	Measured value	Relative error	Value range of the accumulating errors**
Incident power	Background spectrum calibration	0.1973 ± 0.0065	0.00815	-
	Beam intensity distribution calibration	3.3 ± 4 [W]	1.212	1.5~7.4 μ W
Absorbed power	Frequency response calibration*	1.314 ± 0.162 [mW · μ m]	0.1233	-
	Power calibration	0.3307 ± 0.017 mW	0.0514	-
$\frac{\text{Absorbed power}}{\text{Incident power}}$	Absorptance peak (11 μ m)	$48.66 \pm 4.85\%$	0.100	21.29~105.0%

*To quantify the error of the frequency response calibration, the absolute absorbed power spectra of Fig. 4-7 are considered, and the peak absorbed power of 11 μ m are chosen as the indication.

**The value range of the accumulating errors indicates the previous measurement errors will have influence on this measurement, and the upper and lower limits are provided.

Chapter 5

Conclusion

5.1 Summary

The measurement platform disclosed in this thesis enables the measurement of quantitative broadband absorptance spectra on micro/nano-scaled samples. By combining an interferometer with a micro fabricated bilayer cantilever beam, the broadband absorptance spectrum of a sample can be measured in a single scan using Fourier Transform Spectroscopy. Compared to conventional dispersive spectrometers, this platform fundamentally allows for faster data acquisition, greater spectral resolution and a higher signal-to-noise ratio. In addition, the use of a bilayer cantilever probe as the principle thermal sensor enables direct and quantitative measurement of absorptance spectra with picowatt sensitivity. Thus this platform is one of the few capable of characterizing micro- and even nanometer-sized samples. Given the inherent robustness of this platform, it is believed that such a system can be easily integrated into existing FTIR or FTVIS systems as an accessory.

5.2 Extension of Prior Art

Experimental results presented so far are based on commercially available cantilevers. It should be emphasized that different variations of the cantilever-based sensor can also be used in this system. For example, a new structural design, which consists of a bi-arm cantilever platform that decouples the sample arm and the probe arm,²⁴ was recently disclosed. Fig. 5-1 shows an optical microscope image of this bi-arm cantilever. The probe arm is composed of a silicon nitride (SiN_x) substrate with a gold (Au) coating. The sample arm is made up of only SiN_x with an Au reflective coating at its tip for sensing and optical heating. This coating does not affect the deflection response of the detector arm. There are three reasons for decoupling the detector arm and the sample arm. First, by isolating the sample arm from the detector arm, any errors caused by the detector arm absorbing stray input light can be avoided. Second, since the sample arm is not bilayer, its alignment to the input light source will remain static despite variations in the heat input. Third, due to the lower thermal conductivity of SiN_x compared with metals, the absorbed power coming from the sample arm can generate a higher temperature difference, resulting in a thermal detector with a higher sensitivity. Once again, the platform developed in this thesis is compatible with different cantilever designs, including variations of this particular bi-arm sensor.

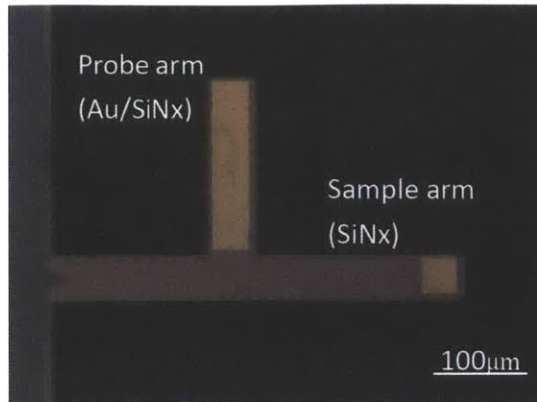


Figure 5-1 : SiNx/Au bi-arm cantilever sensor. This platform decouples the sample arm and the probe arm.

5.3 Future Works

The demonstration of this new system can directly and quantitatively measure the broadband absorptance from 3 to 18 μm (mid-infrared), and the replacement of the chalcogenide infrared (CIR) fiber can have the access to the range of 2 to 6 μm (near-infrared to mid-infrared). This new system can be a versatile platform to characterize the optical feature in the infrared region combining with the bi-armed cantilever. It can measure the absorptance of the micro/nano-sized samples such as a nanowire,^{45,46} thermal electric powers,^{47,48} patterned or textured surface,^{49,50,51,52} and the study of the interaction between photon and phonon.⁵³

Bibliography

- [1] J. R. Barnes, R. J. Stephenson, M. E. Welland, Ch. Gerber, and J. K. Gimzewski. *Nature*. **372**, 3, 79-81, 1994.
- [2] J. K. Gimzewski, Ch. Gerber, E. Meyer, and R. R. Schlittler. *Chemical Physics Letters*. **217**, 5, 6, 589-594, 1994.
- [3] R. J. Bell, *Introductory Fourier Transform Spectroscopy*. New York: Academic Press, 1972.
- [4] A. Rosencwaig and A. Gersho. *Journal of Applied Physics*. **47**, 1, Jan., 1976.
- [5] T. Schmid. *Analytical Bioanalytical Chemistry*. **384**, 1071-1086, 2006.
- [6] V. Koskinen, J. Fonsen, K. Roth, and J. Kauppinen. *Vibrational Spectroscopy*. **48**, 16-21, 2008.
- [7] S. D. Timoshenko. *J. Opt. Soc. Am.* **2**, 233, 55
- [8] J. Lai, T. Perazzo, Z. Shi, and A. Majumdar. *Sensors and Actuators A*. **58**, 113-119, 1997.
- [9] S. Sadat, Y. J. Chua, W. Lee, Y. Ganjeh, K. Kurabayashi, E. Meyhofer, and P. Reddy. *Applied Physics Letters*. **99**, 043106, 2011.
- [10] J. R. Barnes, R. J. Stephenson, C. N. Woodburn, S. J. O'Shea, M. E. Welland, T. Rayment, J. K. Gimzewski, and C. Gerber. *Review of Scientific Instrument*. **65**, 12, 3793-3798, 1994.
- [11] J. Varesi, J. Lai, T. Perazzo, Z. Shi, and A. Majumdar. *Applied Physics Letters*. **71**, 3, 21, 1997.

- [12] S. Shen, A. Narayanaswamy, S. Goh, and G. Chen. *Applied Physics Letters*. **92**, 063509, 2008.
- [13] S. Shen, A. Narayanaswamy, and G. Chen. *Nano Letters*. **9**, 2909-2913, 2009.
- [14] A. Narayanaswamy and N. Gu. *Journal of Heat Transfer*. **133**, 042401-1, 2011.
- [15] E. T. Arakawa, N. V. Lavrik, and G. Datskos. *Applied Optics*, **42**, 10, 2003.
- [16] P. G. Datskos, S. Rajic, M. J. Sepaniak, N. Lavrik, C. A. Tipple, L. R. Senesac, and I. Datskou. *Journal of Vacuum Science & Technology B*, **19**, 4, 2001.
- [17] R. Mukhopadhyay, V. V. Sumbayev, M. Lorentzen, J. Kjems, P. A. Andreasen, and F. Besenbacher. *Nano Letters*. **5**, 12, 2385-2388, 2005.
- [18] S. Shen, A. Henry, J. Tong, R. Zheng, and G. Chen, *Nature Nanotechnology*, **5**, 251-255, 2010.
- [19] A. Hammiche, H. M. Pollock, M. Reading, M. Claybourn, P. H. Turner, and K. Jewkes. *Applied Spectroscopy*. **53**, 7, 1999.
- [20] A. Hammiche, L. Bozec, M. J. German, J. M. Chalmers, N. J. Everall, G. Poulter, M. Reading, D. B. Grandy, F. L. Martin, and H. M. Pollock. *Spectroscopy*, **19**, 2, 2004.
- [21] A. Dazzi, R. Prazeres, F. Glotin, and J. M. Ortega. *Optics Letters*. **30**, 18, 2005.
- [22] C. Prater, K. Kjoller, D. Cook, R. Shetty, G. Meyers, C. Reinhardt, J. Felts, W. King, K. Vodopyanov, and A. Dazzi. *Microscopy and Analysis*. **24**, 3, 5-8, 2010.
- [23] B. R. Burg, J. K. Tong, W. C. Hsu, P. L. Sambegoro, A. Mavrokefalos, and G. Chen. *Decoupled Cantilever Arms for Optomechanical Thermal Measurements*, U.S. Patent Application No.:61/599547, Feb, 2012.
- [24] P. R. Griffiths, J. A. De Haseth. *Fourier Transform Infrared Spectroscopy*. John Wiley & Sons, New York, 1986
- [25] M. Born and E. Wolf. *Principles of Optics*. 7th ed. Cambridge University Press, UK, 1999.

- [26] A. Ghatak. Optics. 4th ed. McGraw-Hill, New Delhi, 2009.
- [27] E. Hecht, A. R. Ganesan. Optics. 4th ed. Pearson, USA, 2002.
- [28] L. J. Vandergriff, F. Seeper, L. S. Pedrotti, L. S. Pedrotti, W. T. Silfvast, J. Ready, A. Ghatak, K. Thyagarajan, N. Massa, H. R. Myler, and T. H. Jeong. *Fundamentals of Photonics*. SPIE Press, 2008.
- [29] D. Marcuse. *Journal of the Optical Society of America*. **68**, 1, 103-109, 1978.
- [30] J. K. Patel, C. B. Read. *Handbook of the Normal Distribution*, 2nd ed. Marcel Dekker, Inc., New York, 1996.
- [31] B. Kwon, M. Rosenberger, R. Bhargava, D. G. Cahill, and W. P. King. *Review of Scientific Instruments*. **83**, 015003, 2012.
- [32] A. F. Mills. *Heat Transfer*. 2nd ed. Richard D. Irwin. Inc., USA, 1992.
- [33] P. G. Datskos, N. V. Lavrik, S. Rajic. *Review of Scientific Instruments*. **75**, 4, 1134-1148, 2004.
- [34] A. Khan, J. Philip, and P. Hess. *Journal of Applied Physics*. **95**, 4, 1667-1672, 2004.
- [35] H. J. Butt, and M. Jaschke. *Nanotechnology*. **6**, 1-7, 1995.
- [36] H. Sadeghian, C. K. Yang, J. F. L. Goosen, E. van der Drift, A. Bossche, P. J. French, and F. van Keulen. *Applied Physics Letters*. **94**, 221903, 2009.
- [37] K. E. Petersen. *Proceedings of the IEEE*. **70**, 5, 420-457, 1982.
- [38] B. Bhushan and X. Li. *Journal of Materials Research*. **12**, 1, 54-63.
- [39] P. G. Datskos, N. V. Lavrik, S. Rajic. *Review of Scientific Instruments*. **75**, 4, 1134-1148, 2004.
- [40] R.O.E. Vijgen, and J.H. Dautzenberg. *Thin Solid Films*. **270**, 264-269, 1995.
- [41] G. Chen. *Nanoscale Energy Transport and Conversion*. Oxford, New York, 2005.
- [42] A. Wig, A. Passian, E. Arakawa, T. L. Ferrell, and T. Thundat. *Journal of Applied Physics*. **95**, 3, 2004.

- [43] B. J. Lee and Z. M. Zhang. *13th International Conference on Advanced Thermal Processing of Semiconductors, IEEE*. 0-7803-9223-X/05, 2005.
- [44] S. M. Sze and K. K. Ng. *Physics of Semiconductor Devices*. Wiley, New Jersey, 2007.
- [45] L. Cao, J. S. White, J. S. Park, J. A. Schuller, B. M. Clemens, and M. L. Brongersma. *Nature Materials*. **8**, 643-647, 2009.
- [46] J. Giblin, M. Syed, M. T. Banning, M. Kuno, and G. Hartland. *Nano*. **4**, 1, 358-364, 2010.
- [47] J. Navratil, J. Horak, T. Plechacek, S. Kamba, P. Lostak, J. S. Dyck, W. Chen, and C. Uher. *Journal of Solid State Chemistry*. **177**, 1704-1712, 2004.
- [48] Y. S. Hor, A. Richardella, P. Roushan, Y. Xia, J. G. Checkelsky, A. Yazdani, M. Z. Hasan, N. P. Ong, and R. J. Cava. *Physical Review B*, **79**, 195208, 2009.
- [49] A. Mavrokerfalos, S. E. Han, S. Yerci, M. S. Branham, and G. Chen. *Nano Letters*. **12**, 6, 2792-2796, 2012.
- [50] S. E. Han and G. Chen. *Nano Letters*. **10**, 11, 4692-4696, 2010.
- [51] B. Yan, S. V. Boriskina, and B. M. Reinhard. *Journal of Physical Chemistry C*. **115**, 24437-24453, 2011.
- [52] W. Ahn, S. V. Boriskina, Y. Hong, and B. M. Reinhard. *Nano Letters*. **12**, 1, 219-227, 2011.
- [53] L. Alekseyev, E. Narimanov, and J. Khurgin. *Optics Express*. **19**, 22, 22350-22357, 2011.